

Multicomponent adsorption in mesoporous flexible materials with flat-histogram Monte Carlo methods

Nathan A. Mahynski and Vincent K. Shen

Citation: *The Journal of Chemical Physics* **145**, 174709 (2016); doi: 10.1063/1.4966573

View online: <http://dx.doi.org/10.1063/1.4966573>

View Table of Contents: <http://scitation.aip.org/content/aip/journal/jcp/145/17?ver=pdfcov>

Published by the [AIP Publishing](#)

Articles you may be interested in

[Elucidating the effects of adsorbent flexibility on fluid adsorption using simple models and flat-histogram sampling methods](#)

J. Chem. Phys. **140**, 244106 (2014); 10.1063/1.4884124

[Accelerating flat-histogram methods for potential of mean force calculations](#)

J. Chem. Phys. **131**, 054105 (2009); 10.1063/1.3183165

[Adsorption/desorption hysteresis of simple fluids confined in realistic heterogeneous silica mesopores of micrometric length: A new analysis exploiting a multiscale Monte Carlo approach](#)

J. Chem. Phys. **127**, 154701 (2007); 10.1063/1.2790423

[Adsorption of 1-octanol at the free water surface as studied by Monte Carlo simulation](#)

J. Chem. Phys. **120**, 11839 (2004); 10.1063/1.1753255

[Transition Matrix Monte Carlo and Flat-Histogram Algorithm](#)

AIP Conf. Proc. **690**, 344 (2003); 10.1063/1.1632146



**Pure Metals • Ceramics
Alloys • Polymers**
in dozens of forms

Goodfellow

Small quantities *fast* • Expert technical assistance • 5% discount on online orders

Multicomponent adsorption in mesoporous flexible materials with flat-histogram Monte Carlo methods

Nathan A. Mahynski^{a)} and Vincent K. Shen

Chemical Sciences Division, National Institute of Standards and Technology, Gaithersburg, Maryland 20899-8320, USA

(Received 29 July 2016; accepted 17 October 2016; published online 7 November 2016)

We demonstrate an extensible flat-histogram Monte Carlo simulation methodology for studying the adsorption of multicomponent fluids in flexible porous solids. This methodology allows us to easily obtain the complete free energy landscape for the confined fluid-solid system in equilibrium with a bulk fluid of any arbitrary composition. We use this approach to study the adsorption of a prototypical coarse-grained binary fluid in “Hookean” solids, where the free energy of the solid may be described as a simple spring. However, our approach is fully extensible to solids with arbitrarily complex free energy profiles. We demonstrate that by tuning the fluid-solid interaction ranges, the inhomogeneous fluid structure inside the pore can give rise to enhanced selective capture of a larger species through cooperative adsorption with a smaller one. The maximum enhancement in selectivity is observed at low to intermediate pressures and is especially pronounced when the larger species is very dilute in the bulk. This suggests a mechanism by which the selective capture of a minor component from a bulk fluid may be enhanced. [<http://dx.doi.org/10.1063/1.4966573>]

I. INTRODUCTION

Adsorption of fluids into porous media is a process of both fundamental interest and practical significance for many fields including gas storage and sequestration,^{1,2} catalysis,³ drug delivery,⁴ and separations.^{5,6} In particular, adsorption-based separations of multicomponent fluid mixtures represent an important alternative to numerous industrial processes such as distillation, which are significantly more energy intensive.^{6,7} Many fundamental studies of adsorption have been undertaken over the past century in an effort to understand the details of the corresponding molecular-level processes. Density functional theories^{8,9} and molecular simulation have emerged as some of the primary tools for modeling and understanding adsorption at the molecular level.¹⁰ Mean-field approaches often struggle to accurately capture the impact of confinement and solution non-idealities on the structure and correlations between components and so direct simulation is traditionally used to benchmark these methods.^{11–18} Monte Carlo simulation is particularly well-suited for studying fluid adsorption, and it is a computationally efficient approach for determining the thermodynamic properties of these confined systems.^{10,19} However, the computational cost involved in studying multicomponent mixtures often increases greatly with the number of components present, making simplified theoretical approaches seem more practical.^{18,20,21} Unfortunately, these simplifications also make it difficult to accurately capture a number of system details because of underlying assumptions.

For instance, the consequences of adsorbent flexibility are often neglected in many simplified theoretical models of multicomponent adsorption, such as Ideal Adsorbed

Solution Theory (IAST).²⁰ It is well-known that many adsorbents including carbons,^{12,22,23} silicas,^{24–26} and metal-organic frameworks (MOFs)^{2,27–30} exhibit deformation under adsorption stress. Because the adsorbent itself deforms in response to stimuli provided by the adsorbing fluid, the adsorbent must be considered as a part of the system whose thermodynamic behavior is now a function of $N + 1$ species, where the fluid contains N components. To remedy this, an osmotic framework extension of this theory was developed to account for the stress imposed by the adsorbate fluid on the adsorbing material, which has recently been implemented in a number of theoretical treatments and in some molecular simulations.^{19,31–35} However, many of these theoretical implementations rely on the knowledge of an equation of state for individual components and assume relatively ideal mixing; non-idealities may be incorporated in principle, but the resulting accuracy relies on the choice of a good model which is not always obvious.³¹

In general, one can divide the types of adsorbent flexibility into two classes (cf. Fig. 1). First, the strain the adsorbent experiences due to the fluid-induced adsorption stress can result in a macroscopic volume change of the adsorbent, e.g., the swelling of clays or “breathing” of certain MOFs.^{27,36–38} Conversely, the adsorption stress can cause the adsorbent material to undergo conformational changes which do not change the material’s macroscopic volume but instead modify its internal structure or accessible volume, such as the “gate-opening” transition in ZIF-8 or the rotation of surface functional groups.^{26,28,30,39,40} The presence of intermediate and metastable structures in these transitions is a complication that requires knowledge of the free energy landscape to properly understand.

Flat-histogram Monte Carlo methods are advantageous as they can efficiently construct this landscape and provide

^{a)}Electronic mail: nathan.mahynski@nist.gov

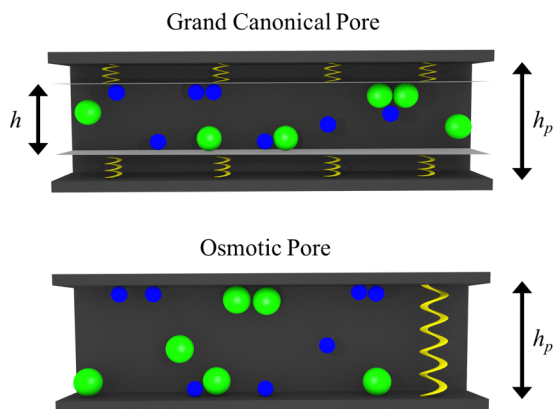


FIG. 1. Schematic of the adsorption of a binary fluid mixture in a flexible slit pore. In the grand canonical pore ensemble, the macroscopic material volume (Ah_p) is fixed while internally the material may deform. In the osmotic pore ensemble, the macroscopic volume can change and we set $h_p = h$.

a complete thermodynamic description of the adsorption process, including all information about stable and metastable states. A principal advantage of the recently developed framework by Shen and Siderius¹⁹ for studying adsorption in flexible single-component systems using this approach is the ability to construct different free energy landscapes after simulations have been completed; this is done by imposing different free energy profiles for the empty solid adsorbent in the limit of zero pressure to self-consistently combine results from different simulations. This permits the study of multitudes of different realistic and hypothetical materials to screen for advantageous properties conferred by the material's flexibility with minimal computational effort. However, previous works have focused on the adsorption of single component fluids in flexible materials due to the computational cost and complexity of introducing additional components.¹⁹ In this work, we adapt other previously developed, flat-histogram-based methods for efficiently obtaining the thermodynamic properties of bulk multicomponent fluids^{41,42} to multicomponent fluids confined in flexible adsorbents. The result is an extensible framework for obtaining the free energy landscape of multicomponent fluid mixtures adsorbed in materials with arbitrary flexibilities.

For simplicity, we demonstrate this methodology for binary supercritical fluids adsorbed in a slit pore whose flexibility can be described by an effectively Hookean spring. Future contributions will focus on subcritical temperatures in which bulk phase transitions and capillary condensations can occur, as well as more complex materials. We demonstrate this framework for both classes of flexibilities and systematically investigate the consequences of tuning the interactions between the adsorbent and each component in the mixture. We focus on a simple fluid representative of classes of binary mixtures which are relatively difficult to separate through conventional distillation processes. This makes adsorption an attractive alternative if the adsorbent's properties can be appropriately tuned. Coarse-grained interactions between fluid components and an adsorbent, such as the 10-4-3 Steele potential⁴³ often have their effective interaction range

determined by the molecular size of the adsorbate. However, with the advent of advanced chemical synthesis techniques, particularly in MOFs,^{44,45} and in the interest of better understanding design principles, it is worth reconsidering models which have interaction ranges decoupled from their molecular size. We systematically vary the strength and range of the fluid-adsorbent interactions to understand the impact that this has on the heterogeneous fluid structure and resulting adsorption selectivity.

The remainder of this paper is organized as follows. In Sec. II, we describe how material flexibility is modeled, the two thermodynamic ensembles which represent the different classes of flexible materials, and our simulation approach. We apply our approach to study binary fluid adsorption in these flexible materials and discuss the results in Sec. III. Section IV summarizes our conclusions and provides an outlook for future work, while Appendices A–E contain a complete derivation of our methodology and additional details of its implementation.

II. METHODS

A. Pore flexibility

In this work, we modeled a flexible mesoporous adsorbent material at the individual pore level. For simplicity, our simulations employed a slit-pore as described in Fig. 1; however, our approach is general and applies to more complex pore geometries as long as their size can be represented with a scalar variable. For a slit-pore geometry, only the pore width, h , is deformable, while its cross-sectional area, A , is fixed. The canonical partition function for a single pore in such a solid is given by

$$Q_s(h) = \frac{1}{\Lambda_s^{3N_s} N_s!} \int_{V=Ah} \mathbf{dr}^{N_s} \exp(-\beta U_{s,s}(h)), \quad (1)$$

where $\beta \equiv 1/k_B T$ (k_B is the Boltzmann constant), Λ_s refers to the thermal de Broglie wavelength, N_s is the number of (fictitious) atoms or molecules comprising the pore, and $U_{s,s}$ is the potential energy resulting from interactions between the pore's molecules. The free energy of the material in the absence of any adsorbate is only a function of h and is simply related to this partition function by

$$F_s(h) = -k_B T \ln Q_s(h). \quad (2)$$

The isothermal bulk modulus is defined as $K_T = -V (\partial P / \partial V)_{T, N_s}$. Here we take V as referring to the material volume which changes in response to stress. In breathing materials, this is simply an adsorbent's overall macroscopic volume; whereas in gate-opening materials this refers to the adsorbent volume inaccessible to the adsorbate. Using the fundamental equation for this material in the canonical ensemble, this can be rewritten as a second derivative of the material's free energy,

$$K_T = V \left(\frac{\partial^2 F_s}{\partial V^2} \right)_{T, N_s}. \quad (3)$$

Throughout this work, we chose $F_s(h)$ to be a parabola reminiscent of an effectively Hookean spring, whose second

derivative is well defined with respect to its spring constant, k , and an equilibrium pore width, h_0 ,

$$F_s(h) = k(h - h_0)^2. \quad (4)$$

Hence, we report the product $K_T A$, which is simply related to the effective spring constant of the material via

$$K_T A = 2hk. \quad (5)$$

In our convention, we report $K_T A$ at the equilibrium pore size when no adsorbate is present, $h = h_0 = 8\sigma_{2,2}$, where $\sigma_{2,2}$ represents the molecular diameter of the second, smaller species. When the adsorbent is loaded with adsorbate, the interaction of the material's fictitious molecules with each other is assumed to be independent of the adsorbate. This implies that the total canonical partition function for the binary adsorbate-adsorbent composite system is given by

$$Q(h) = Q_s(h)Q_f \quad (6)$$

$$= \exp(-\beta F_s(h))Q_f, \quad (7)$$

where $Q_s(h)$ is given by Eq. (1) and Q_f refers to the partition function describing all fluid-based interactions including the adsorbate-adsorbate and adsorbate-adsorbent effects. The adsorbent-adsorbent interactions are wholly contained within Q_s which is determined by the choice of $F_s(h)$.

B. Thermodynamic ensembles

In this work, we considered the confined fluid under two ensembles: the “grand canonical pore” and “osmotic pore” ensembles. The former refers to a system under the constraints of fixed fluid chemical potentials, adsorbent mass, temperature, and macroscopic pore volume $V = Ah_p$ (cf. Fig. 1). In this ensemble, changes to the adsorbent's internal degrees of freedom change the volume inside the material accessible to the adsorbate, but not the material's macroscopic volume. This is a representative of gate-opening materials such as ZIF-8, which rearranges its internal structure upon sufficient adsorbate loading to increase the volume available to the adsorbate; however, this change has no effect on the overall dimensions of the MOF. In the grand canonical pore case, the fundamental equation is given by

$$d \ln \Xi = -Ud\beta + \beta PdV + N_1 d(\beta\mu_1) + N_2 d(\beta\mu_2) - \beta\mu_s dN_s, \quad (8)$$

where $\Xi(\beta, V, \mu_1, \mu_2, N_s)$ is the grand partition function, U is the internal energy, P is the net pressure, μ_i is the chemical potential of species i , and N_i is the number of molecules of species i present. The subscript “ s ” refers to the solid adsorbent. This can be related to its free energy, Ω , through the appropriate bridge function

$$\ln \Xi(\beta, V, \mu_1, \mu_2, N_s) = \beta PV - \beta\mu_s N_s = -\beta\Omega. \quad (9)$$

In this ensemble, we define a macrostate of the system based on the instantaneous pore size, h , and the total number of adsorbate molecules present, N_{tot} . From a statistical mechanical perspective, the probability of observing a

macrostate is given by

$$\Pi_{\text{gc}}(h, N_{\text{tot}}) = \frac{\exp(-\beta F_s(h) + \beta\mu_1 N_{\text{tot}}) \Upsilon(\Delta\mu_2)}{\Xi}, \quad (10)$$

where Υ is the isochoric semigrand partition function (cf. Appendix A) which is a function of $\Delta\mu_2 \equiv \mu_2 - \mu_1$.

Conversely, in the osmotic pore ensemble, the adsorbent is assumed to have no internal degrees of freedom. Instead, the material's macroscopic volume fluctuates in response to adsorption stress. This ensemble captures the thermodynamics of flexible adsorbents such as MIL-53, which deforms upon adsorbate loading, resulting in a change to the adsorbent's macroscopic volume while maintaining its molecular “wine-rack” motif. In this case, the fundamental equation is given by

$$d \ln \Gamma = -Ud\beta - Vd(\beta P) + N_1 d(\beta\mu_1) + N_2 d(\beta\mu_2) - \beta\mu_s dN_s, \quad (11)$$

where the osmotic partition function, $\Gamma(\beta, P, \mu_1, \mu_2, N_s)$, is similarly related to the free energy in this ensemble via its bridge function

$$\ln \Gamma(\beta, P, \mu_1, \mu_2, N_s) = -\beta\mu_s N_s = -\beta\Psi. \quad (12)$$

For the osmotic pore ensemble, the probability of observing a given macrostate is

$$\Pi_{\text{os}}(h, N_{\text{tot}}) = \frac{\exp(-\beta F_s(h) - \beta PAh + \beta\mu_1 N_{\text{tot}}) \Upsilon(\Delta\mu_2)}{\Gamma}. \quad (13)$$

We refer the interested reader to, e.g., Refs. 31 and 19 for more detailed discussions of these ensembles.

C. Simulations

To obtain the thermodynamic properties, we employed computationally efficient flat-histogram Monte Carlo methods to compute the macrostate probability distribution, $\ln \Pi(h, N_{\text{tot}})$, for confined systems in equilibrium with a reservoir of adsorbate at a fixed mole fraction (isopleths). Specifically, we used a combination of Wang-Landau and Transition Matrix Monte Carlo methods (cf. Appendix B). One of the key advantages of our approach comes from the fact that we have expressed macrostate probabilities (Eqs. (10) and (13)) in terms of $\Upsilon(\Delta\mu_2)$. This allows us to treat the probabilities as a function of a single scalar variable, N_{tot} , which is used in our biased Monte Carlo sampling methods. Previous work has shown this to be an efficient way to compute the bulk thermodynamic properties of multicomponent fluids when only concerned with first order transitions, i.e., those characterized by changes to N_{tot} .⁴¹ Similarly, this approach generalizes our simulation methodology to an arbitrary number of adsorbate components, significantly increasing the computational efficiency of these methods for confined multicomponent systems. In Appendices A–E, we describe how we obtained $\ln \Pi(N_{\text{tot}})$ from fixed-volume flat-histogram simulations. In what follows, we assume this is a known quantity and simply summarize the construction of the joint distribution, $\ln \Pi(h, N_{\text{tot}})$, and subsequent calculations.

TABLE I. Square-well interaction parameters for both the single component and binary systems.

i	j	$\epsilon_{i,j}$	$\sigma_{i,j}$	$\lambda_{i,j}$
1	1	1.20	1.50	1.33
1	2	1.10	1.25	1.40
2	2	1.00	1.00	1.50

1. Model interactions

All species interacted with each other through a radially isotropic square-well potential given by

$$U_{i,j}(r) = \begin{cases} \infty, & r \leq \sigma_{i,j} \\ -\epsilon_{i,j}, & \sigma_{i,j} < r \leq \lambda_{i,j}\sigma_{i,j} \\ 0, & \lambda_{i,j}\sigma_{i,j} < r \end{cases} \quad (14)$$

Parameters for each species are listed in Table I. The self-interaction parameters of the second component, $\epsilon_{2,2} = \sigma_{2,2} = 1.00$, were used to non-dimensionalize all energy and length scales, respectively, unless otherwise stated. Each pure component undergoes a liquid-vapor phase separation upon cooling. The critical temperature for species 1 is $k_B T_{c,1}/\epsilon_{2,2} \approx 1.1$, while for species 2, $k_B T_{c,2}/\epsilon_{2,2} \approx 1.2$ (cf. Appendix E). To remain supercritical and avoid any finite-size effects, all simulations in this work were performed at $T^* \equiv k_B T/\epsilon_{2,2} = 1.35 > T_{c,2}^* > T_{c,1}^*$. The cross interaction between different species was determined using the standard Lorentz-Berthelot mixing rules $\epsilon_{i,j} = \sqrt{\epsilon_{i,i}\epsilon_{j,j}}$, $\sigma_{i,j} = (\sigma_{i,i} + \sigma_{j,j})/2$. The bulk phase diagram for this mixture is depicted in Fig. 2.

The relatively narrow phase envelope implies that attempting to separate such a mixture using distillation would be somewhat cumbersome, owing to the number of stages it would require.⁴⁶ Thus, although this mixture is not based on any specific fluid, it represents a prototypical mixture that would be a good candidate for separation by adsorption. Furthermore, a number of highly miscible binary mixtures are known to exhibit surprisingly strong spatial segregation under confinement leading to “microphase separation”;^{47–49} this process is not yet well understood and we anticipate that our investigation may shed light on this phenomenon.

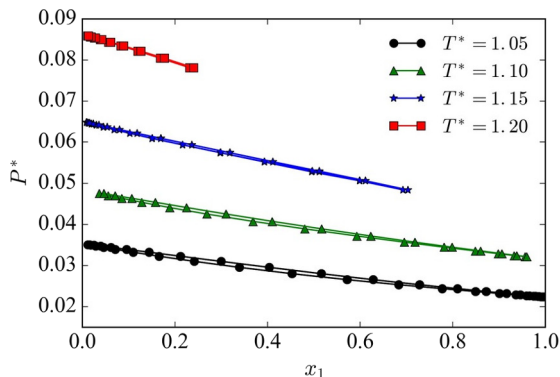


FIG. 2. Bulk phase diagram for the binary fluid investigated here. Reduced pressure, P^* , is plotted against the mole fraction of species 1, x_1 (cf. Eq. (16)). No phase equilibrium was found for $T^* = 1.25$ or higher.

In our simulations, there were two structureless walls fixed in the x - y plane of the simulation box at $z = \pm h/2$. The simulation box was large enough in the z -direction to prevent interactions with periodic images in this direction. For $-h/2 \leq z \leq h/2$, the interaction of a fluid particle with a wall was also treated via a square well potential

$$U_{i,w}(z) = \begin{cases} \infty, & |z - h_z| \leq \sigma_{i,i}/2 \\ -\epsilon_{i,w}, & \sigma_{i,i}/2 < |z - h_z| \leq \lambda_{i,w}\sigma_{i,i} \\ 0, & \lambda_{i,w}\sigma_{i,i} < |z - h_z| \end{cases} \quad (15)$$

where h_z indicates the wall bounds, one at $z = h/2$ and another at $z = -h/2$. Beyond these bounds ($|z| > h/2$) the energy was also infinite.

2. Parameterizing bulk isopleths

Here we wish to consider the adsorption behavior of a bulk fluid with a fixed composition as its pressure is increased. To do so, we obtained the macrostate distribution from a series of different grand canonical Monte Carlo simulations. This was then used to construct a parameterized curve of (μ_1, μ_2) defining fixed bulk composition as a function of pressure. For many multicomponent simulation approaches, this is often difficult to obtain and simple assumptions are made to estimate this curve. For example, one can simply fix the difference in chemical potentials while increasing the chemical potential of a single species; however, this only yields a true isopleth in the limit of an ideal gas. In fact, the true isopleths are directly available with our approach which represents another principal advantage. First, we computed the macrostate distribution, $\Pi(N_{\text{tot}}; \mu_1, \Delta\mu_2)$, for a bulk fluid at different $\Delta\mu_2$ values by performing a series of grand canonical simulations at $\mu_1^0 = 0$, such that $\mu_2 = \Delta\mu_2$. Once the macrostate probability distribution has been obtained at a given $\Delta\mu_2$, it can be reweighted to any desired μ_1 (cf. Appendix A). At each μ_1 , the mole fraction may be obtained

$$x_1 = \frac{\langle N_1 \rangle}{\langle N_{\text{tot}} \rangle} = \frac{\sum_{N_{\text{tot}}} N_1(N_{\text{tot}})\Pi(N_{\text{tot}})}{\sum_{N_{\text{tot}}} N_{\text{tot}}\Pi(N_{\text{tot}})}, \quad (16)$$

where $N_1(N_{\text{tot}})$ was collected as a histogram during the simulations at $\mu_1 = \mu_1^0$. By collecting the results for all points in the grid of $\Delta\mu_2$ values, one can interpolate to construct a surface of $x_1(\mu_1, \Delta\mu_2)$ as shown in Fig. 3, where dashed black lines indicate lines of constant $\Delta\mu_2$. Isopleths may be extracted as the contours along which x_1 is equal to our desired target, shown in the inset of Fig. 3. We refer the interested reader to Appendices C and D for more details. Thus, we were able to accurately parameterize arbitrary isopleths at discrete (μ_1, μ_2) values. This allowed us to quickly and easily investigate the adsorption behavior of a fluid at any arbitrary composition, beyond archetypal “equimolar” mixtures.

3. Constructing the confined fluid’s macrostate distribution

Next, we consider the behavior of the confined system in equilibrium with a bulk fluid at these conditions. A series of

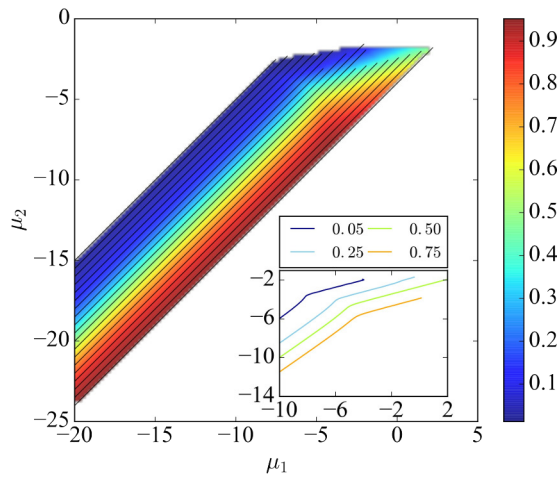


FIG. 3. The surface $x_1(\mu_1, \mu_2)$, or equivalently $x_1(\mu_1, \Delta\mu_2)$, we constructed at $T^* = 1.35$ for the bulk fluid. The estimated mole fraction of species 1 over the range of chemical potentials is shown in color, while contours (isopleths) at $x_1 = 0.05, 0.25, 0.50$, and 0.75 are shown in the inset where the mixtures deviate strongly from ideal gas behavior. Dashed black lines indicate the lines of constant $\Delta\mu_2$ which were simulated to construct this surface.

“rigid pore” grand canonical Monte Carlo simulations were performed at the same grid of $\Delta\mu_2$ values for $\mu_1 = \mu_1^0$ in a slit-pore channel at different fixed h values (cf. Appendix D). From this composite grid, the $\ln \Pi(h, N_{\text{tot}})$ distribution may be “stitched” together after the simulations are complete. For a given (μ_1^t, μ_2^t) along some isopleth, the interpolation of macrostate distributions obtained at neighboring $\Delta\mu_2$ which bracket $\Delta\mu_2^t$ yields $\ln \Pi(N_{\text{tot}}; h, \mu_1^t, \Delta\mu_2^t)$, which can then be reweighted to μ_1^t . This was subsequently repeated for all h values. For a given $F_s(h)$, the composite distribution, $\ln \Pi(h, N_{\text{tot}})$, may be found by imposing self-consistency in the $N_{\text{tot}} = 0$ limit (cf. Eqs. (D7) and (D8)). Typical results for both the grand canonical pore and osmotic pore ensembles are depicted in Fig. 4. With $\ln \Pi(h, N_{\text{tot}})$ known at a given externally imposed condition $(\beta, \mu_1^t, \mu_2^t)$, all properties may be subsequently calculated. As in the previously demonstrated pure component simulation methodology,¹⁹ this permits the construction of the free energy landscape of this multicomponent fluid-adsorbent system for any adsorbent free energy profile without requiring additional simulations.

The extensive properties at a given macrostate (h, N_{tot}) are independent of the probability of observing that macrostate. Therefore, when the grids mentioned above were constructed via rigid pore (or bulk) simulations, we collected histograms of properties including the average potential energy, U , and particle numbers, N_1 and N_2 , as a function of N_{tot} . The average property at a given imposed set of chemical potentials can be calculated by using the reweighted macrostate distribution. This distribution was first normalized such that

$$\sum_h \sum_{N_{\text{tot}}} \tilde{\Pi}(h, N_{\text{tot}}) = 1. \quad (17)$$

Ensemble-averaged extensive properties, $\langle X \rangle$, are simply a weighted average based on the probability of observing a given macrostate

$$\langle X \rangle = \sum_h \sum_{N_{\text{tot}}} \tilde{\Pi}(h, N_{\text{tot}}) X(h, N_{\text{tot}}). \quad (18)$$

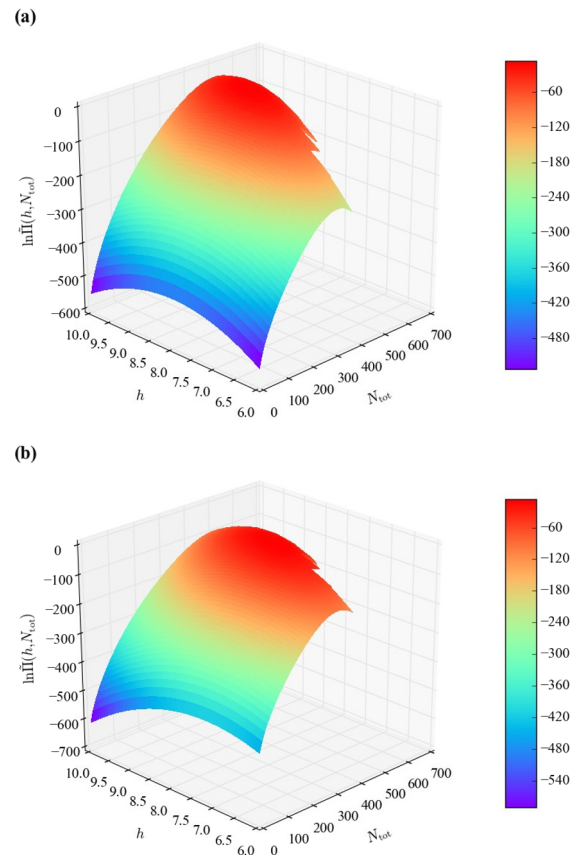


FIG. 4. Representative examples of the normalized macrostate distribution, $\ln \tilde{\Pi}(h, N_{\text{tot}})$, in the (a) grand canonical pore and (b) osmotic pore ensembles. Both distributions were obtained for $\epsilon_{1,w} = \epsilon_{2,w} = 2.50$ for the fluid mixture in Fig. 2 at $T^* = 1.35$ along the $x_1 = 0.05$ isopleth after reweighting to conditions corresponding to a bulk pressure of $P^* = 0.50$.

This calculation was repeated for each (μ_1^t, μ_2^t) point in the bulk isopleth. We emphasize that under the conditions we report here, there exists only one maximum in $\tilde{\Pi}(h, N_{\text{tot}})$ indicating there was only a single stable phase present (cf. Fig. 4).

For progressively smaller pores, the maximum number of adsorbed species is reduced. Hence, $\tilde{\Pi}(h, N_{\text{tot}})$ terminates at smaller N_{tot} values for narrower pores than for wider ones. The edges at low h are visible in Fig. 4. When macrostate distributions were reweighted and combined, these edges were checked such that the difference between the maximum in the macrostate probability and the largest value along the edge of the distribution (“ridge”) was sufficiently large to prevent the edge, or those states beyond the edge, from significantly contributing. Thus, we always ensured that

$$\max[\ln \tilde{\Pi}(h, N_{\text{tot}})] - \max[\ln \tilde{\Pi}(h, N_{\text{tot}})_{\text{ridge}}] > 10. \quad (19)$$

A similar metric was used to determine the terminus of the bulk isopleths in (μ_1, μ_2) space and in all pure component simulations as well. This is especially important when computing the bulk pressure to be used in the construction of the osmotic pore ensemble macrostate distributions. At a given condition, pressure was directly computed from the corresponding bulk macrostate distribution as follows:

$$P_{\text{bulk}} = \frac{\ln \Xi}{\beta V} = \frac{\ln \sum_{N_{\text{tot}}} \Pi(N_{\text{tot}}) / \Pi(0)}{\beta V}. \quad (20)$$

Since the bulk phase and confined phase are in mechanical equilibrium, $P_{\text{bulk}} = P_{\text{pore}} = P$. Throughout this paper, we report pressure in non-dimensional units where $P^* \equiv P\sigma_{2,2}^3/\epsilon_{2,2}$.

III. DISCUSSION

As a demonstration of this methodology, here we consider the adsorption of a binary supercritical fluid in a flexible slit pore as we systematically vary the wall interaction energies and ranges with each component and the material's flexibility to assess the impact of the mesoporous adsorbent's chemical and mechanical properties on its selectivity. We emphasize that in our approach, no assumptions have been made to approximate the isopleths as pressure is increased; they are fully parameterized in terms of the chemical potentials of each species for a bulk fluid at each composition we consider. Representative results are discussed here while the rest have been relegated to the [supplementary material](#) (SM). Additional information on the effects of fluid-fluid interactions may also be found therein.

A. Weak fluid-wall interactions with asymmetric ranges

First, we consider the adsorption of the binary mixture in a slit pore that has relatively weak interactions with both components such that $\epsilon_{1,w} = \epsilon_{2,w} = 2.50$. For this pore we set $\lambda_{1,w} = \lambda_{2,w} = 1.50$. Figure 5 depicts the total number of molecules adsorbed in this pore and the pore's selectivity, when $K_T A = 500$, for various representative isopleths as the pressure of the bulk fluid is progressively increased. Here, and throughout this manuscript unless otherwise stated, solid lines correspond to results obtained in the grand canonical pore ensemble, whereas dashed lines refer to the osmotic pore ensemble. Although the two species have an identical interaction energy with the walls, the larger species has a longer overall interaction range, $\lambda_{1,w}\sigma_{1,1} = 2.25$,

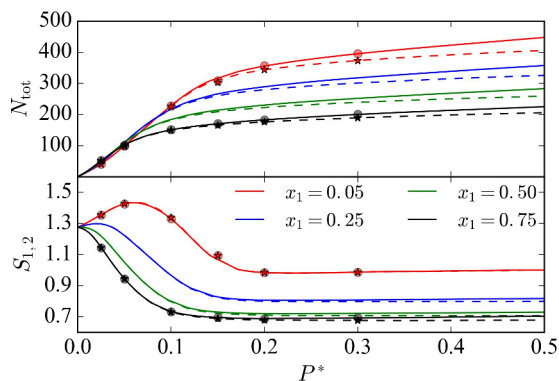


FIG. 5. (Top) Total number of molecules adsorbed in the slit pore for $\epsilon_{1,w} = \epsilon_{2,w} = 2.50$, $\lambda_{1,w} = \lambda_{2,w} = 1.50$ when $K_T A = 500$ along representative isopleths. (Bottom) The corresponding selectivity for species 1 (large) relative to 2 (small). Solid lines correspond to the grand canonical pore ensemble, whereas dashed lines refer to the osmotic pore ensemble. Spheres and stars indicate the pressures at which rigid pore simulations were used to examine the fluid structure within the pore (cf. Fig. 7).

compared to that of the smaller component, $\lambda_{2,w}\sigma_{2,2} = 1.50$. As a result, species 1 has a slightly larger Henry's law coefficient, K_H . In the limit that $P^* \rightarrow 0$, the selectivity, $S_{1,2} = (x_{1,\text{ads}}/x_{1,\text{bulk}})/(x_{2,\text{ads}}/x_{2,\text{bulk}})$, is simply a ratio of the two K_H values¹² which is approximately 1.30 for this mixture. As pressure increases and the pore begins to fill, one expects that packing effects will entropically favor the smaller species, reducing $S_{1,2}$. Indeed, for the bulk isopleths $x_1 \geq 0.25$, Fig. 5 shows precisely this trend. However, for bulk mixtures where species 1 is even more dilute, an intriguing initial non-monotonicity is observed for $P^* \lesssim 0.2$. A representative curve for $x_1 = 0.05$ is shown in Fig. 5 which depicts an initial rise in $S_{1,2}$ which goes through a local maximum before decaying with increasing pressure, as do the rest of the isopleths, in both pore ensembles.

To understand this non-monotonic behavior, we analyzed the structure of the pore and the adsorbed fluid. Figure 6 shows the deformation of the pore in both the grand canonical and osmotic pore ensembles for materials with different bulk moduli. In the former ensemble, when the material is very rigid, $K_T A = 1000$, the material expands linearly by up to approximately 5% over the range of pressures investigated here, regardless of the composition of the bulk adsorbate. Careful inspection reveals that larger x_1 mixtures deform the material marginally less at low pressure and marginally more at higher ones. This trend becomes accentuated as the material's bulk modulus decreases, and begins to show weak oscillations. These pores universally expand under increasing pressure, up to around 10% of their size when empty, h_0 .

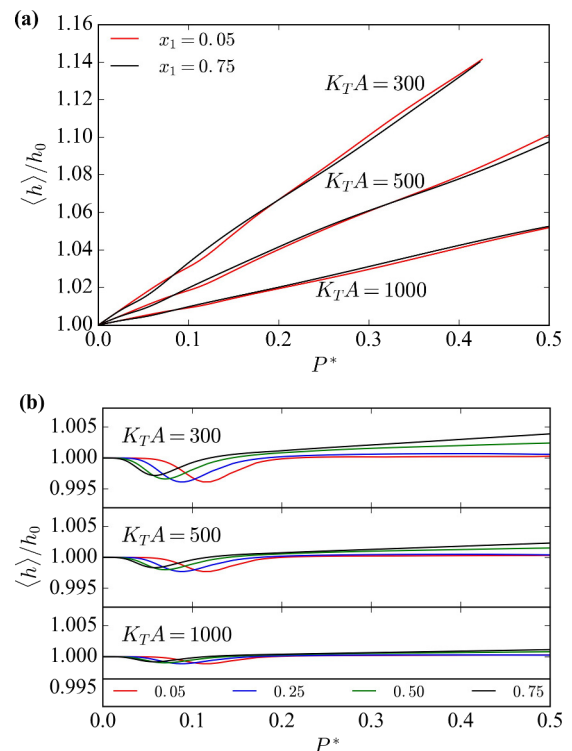


FIG. 6. Pore deformation relative to its equilibrium width when no adsorbate is present (h_0) for the (a) grand canonical pore and (b) osmotic pore ensemble at different flexibilities when $\epsilon_{1,w} = \epsilon_{2,w} = 2.50$, $\lambda_{1,w} = \lambda_{2,w} = 1.50$. Only two representative isopleths are shown in (a) for visual clarity.

Conversely, in the osmotic pore ensemble, the pores show a weak contraction of the order of 1% or less for $P^* \lesssim 0.2$ followed by a weak expansion as the pore fills. The more rigid the material, the less the deformation, as in the grand canonical pore ensemble. It is important to note that the pressures at which the local minima occur in the osmotic pore widths correspond to the troughs in the oscillations that occur in the grand canonical pore ensemble. However, unlike the latter, the former do not display continued oscillations, but rather expand weakly for $x_1 \geq 0.5$ over the pressures depicted in Fig. 6(b).

We then employed grand canonical simulations in rigid pores to evaluate the structure of the adsorbed fluid at various points along the adsorption isotherm, which also traverse the local maximum in $S_{1,2}$. Here the pore width was held fixed at $h = h_0 = 8\sigma_{2,2}$; however, the fact that the adsorption and selectivity curves in Fig. 5 are largely independent of the two pore ensembles, which as indicated by Fig. 6 have different average pore widths, suggests this is not a critical factor. The pore width was divided into one hundred equally sized bins, in which the normalized ensemble-averaged density distribution, $\langle \rho_i(z) \rangle / \langle \rho_{\text{pore}} \rangle = \langle x_i \rangle_{\text{ads}}(z)$, was measured over the course of each simulation; results are depicted in Fig. 7.

The distributions of the two components in the pore when in equilibrium with a bulk fluid at $x_1 = 0.05$ are given in Fig. 7(a). At the lowest pressure, the smaller component (lower

panel) is approximately evenly distributed throughout the region over which it interacts with the wall, while it is relatively dilute in the central region of the pore. The same is true for the larger component (upper panel), although the normalized density decreases marginally very close to the walls as it competes for space with the smaller component, which suffers a smaller entropic penalty than the larger component for existing at the interface. A second layer consisting of the smaller species forms in the interstices of the first ($z/h \approx 0.19, 0.81$) such that it can just interact with the wall, as well as with the first monolayer. Because of entropic considerations owing to its larger size, the larger species tends to be excluded from these layers in favor of forming a third layer atop the bilayer of the smaller component. This is energetically favorable as molecules of the larger component can interact both with the adjacent layer of the smaller species and with the wall since its interaction range is sufficient to extend across these layers.

As the pressure increases further, these effects become more pronounced, and the larger species is gradually expelled from the immediate vicinity of the wall to form increasingly well-defined layers at $z/h \approx 0.25, 0.75$. Closer inspection of the fluid in the inner channel reveals that for $P^* < 0.05$ there is essentially no heterogeneous structure to the fluid in the center of the pore. However, for $P^* \approx 0.10$ oscillations indicate the onset of weakly defined layers, which are especially pronounced for the major component (cf. lower panel of Fig. 7(a)). When $P^* \geq 0.15$, the fluid has formed a well-defined structure which does not change significantly as pressure continues to increase. In fact, $P^* \approx 0.10$ corresponds to the normalized density distribution $\langle x_1 \rangle_{\text{ads}}$ exhibiting the largest maximum in the layer of the larger species (green curve, upper panel). In contrast, when the pore is in equilibrium with a bulk fluid where $x_1 = 0.75$ this behavior does not manifest. The larger species is now in excess and forms layers at the walls in a similar fashion as the smaller species does when it is in excess.

Taken collectively, this reveals the underlying cause of the rise in selectivity of the larger species at an intermediate pressure when the bulk fluid is very dilute in this species ($x_1 = 0.05$). At low pressure, the mixture adsorbs in the pores and is concentrated at the interfaces, where the species in excess tends to form a pair of layers. As pressure increases further, the fluid begins to fill the center of the pore forming a fluid “bridge” between the walls. Just before this bridge is formed, the larger species exhibits a maximum in its local concentration in its principal layer which forms adjacent to the bilayer of the smaller component. Up to this point, the continued adsorption of the smaller species at the walls increasingly provides an energetic benefit to the larger species which adsorbs on top of it. The larger component can interact both with the wall as well as with the smaller component in the layer immediately adjacent to it. Because it is smaller, species 2 can pack more densely in its layer which thus provides a region of high (favorable) energy density for the larger component to adsorb on. This cooperative adsorption behavior is possible primarily because of the range of interactions in the system, rather than the strength of any individual one. Once the bridge has begun to form, the propensity of the larger species

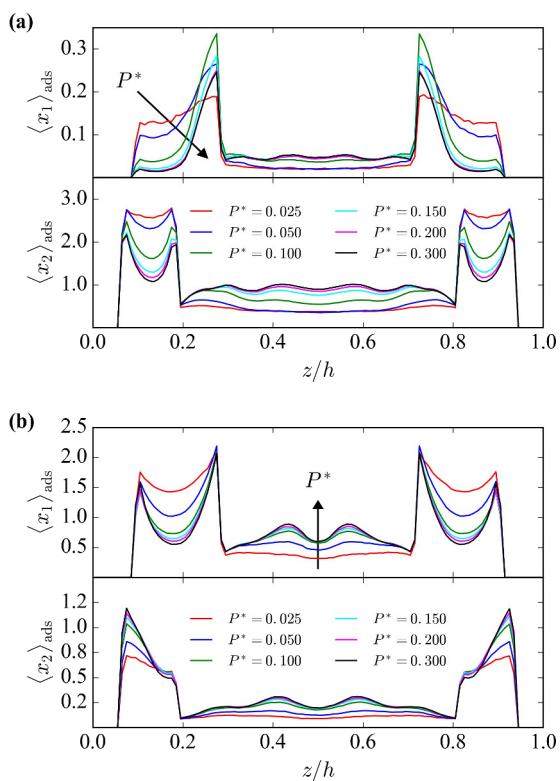


FIG. 7. Normalized ensemble-averaged density distribution, $\langle x_i \rangle_{\text{ads}} = \langle \rho_i(z) \rangle / \langle \rho_{\text{pore}} \rangle$, of each species for $\epsilon_{1,w} = \epsilon_{2,w} = 2.50$, $\lambda_{1,w} = \lambda_{2,w} = 1.50$. The pore width is fixed at $h = h_0 = 8\sigma_{2,2}$ and the pressures depicted correspond to those indicated in Fig. 5. Arrows indicate increasing pressure. (a) Distribution throughout the pore for the isopleth $x_1 = 0.05$ for (top) species 1 and (bottom) species 2. (b) Distribution throughout the pore for the isopleth $x_1 = 0.75$ for (top) species 1 and (bottom) species 2.

to adsorb primarily in a layer adjacent to the bilayer of smaller species is reduced. This is because the increasing density in the pore's interior increases (decreases) the average number of neighbors (potential energy) of a particle located there. It is clear from Fig. 7 that once $P^* \approx 0.15$ a well-defined heterogeneous structure has emerged and changes little as pressure is increased further. For $P^* \geq 0.10$ entropic (packing) considerations begin to impact the adsorption of the larger species, and indeed, lead to a reduction of $S_{1,2}$ as pressure increases further. In the osmotic pore ensemble, the formation of the fluid bridge imposes a correlation between the walls leading to a contraction of the material. At this temperature ($T^* = 1.35$), this is not due to capillary condensation, but is expected to be a precursor to it. In the grand canonical pore, the material expands even at low pressure, but the formation of the bridge reduces the rate of expansion. Subsequent oscillations in $\langle h \rangle$ correspond to the additional layer formation and structural heterogeneity in the pore's interior (cf. Fig. 6). In contrast, for a bulk fluid with a greater concentration of the larger component, e.g., $x_1 = 0.75$, the larger species forms a bilayer at the walls. Any additional layers of the larger species can only interact with the layer immediately adjacent to it, but not additionally with the wall due to its molecular size. The minor component, the smaller species 2, still adsorbs at the wall, but the second layer of the larger species also prevents a third layer of the larger component from interacting with this interior layer of smaller species for the same reason.

Thus, when the larger component is sufficiently dilute so as to allow the smaller component to primarily interact with the walls, the system maximizes its contacts (minimizes energy) by forming a sequence of layers which, before the interior of the pore has any significant concentration, provides a region of high favorable interaction energy leading to a rise in the selective capture of the dilute, large component. It is worth pointing out that similar local maxima in $S_{1,2}$ have been previously reported in mesoporous rigid materials adsorbing supercritical binary mixtures of, for instance, methane and ethane.¹² However, this is often attributed to favorable self-interactions between the same species in which the adsorption of a molecule at the interface enhances further adsorption of the same component, eventually covering the wall and screening its interaction with additional layers. As a result, in those cases the maximum in selectivity of the larger (more strongly interacting) component decreases as its concentration in the bulk decreases. In this system, the cooperative adsorption between different species produces the opposite trend.

B. Weak fluid-wall interactions with symmetric ranges

To further assess this, we consider the consequences of reducing the interaction range of the larger species, such that $\lambda_{1,w} = 1.00$ ($\lambda_{2,w} = 1.50$), making the total range of interaction with the boundaries identical for both species, $\lambda_{1,w}\sigma_{1,1} = \lambda_{2,w}\sigma_{2,2} = 1.50$. Thus, both species must directly compete in the same region next to the walls for adsorption "sites." The adsorption and selectivity curves are shown in Fig. 8. The adsorption isotherms are very similar to the

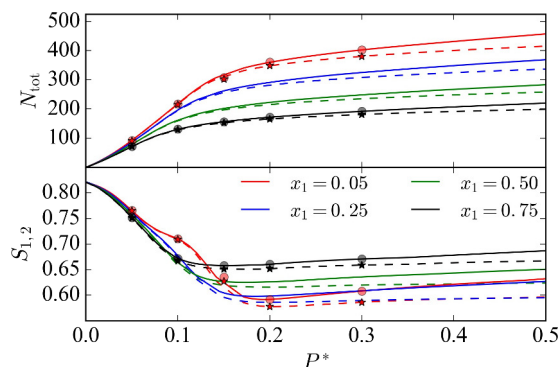


FIG. 8. (Top) Total number of molecules adsorbed in the slit pore for $\epsilon_{1,w} = \epsilon_{2,w} = 2.50$, $\lambda_{1,w} = 1.00$, $\lambda_{2,w} = 1.50$ when $K_T A = 500$ along representative isopleths. (Bottom) The corresponding selectivity for species 1 (large) relative to 2 (small). Solid lines correspond to the grand canonical pore ensemble, whereas dashed lines refer to the osmotic pore ensemble. Spheres and stars indicate the pressures at which rigid pore simulations were used to examine the fluid structure within the pore (cf. Fig. 9).

case where $\lambda_{1,w} = 1.50$. However, the previously observed maximum in $S_{1,2}$ for the bulk isopleth $x_1 = 0.05$ has been reduced to a simple "shoulder" around $P^* = 0.10$. In the limit of zero pressure (empty adsorbent), the selectivities also all begin from $S_{1,2} \approx 0.81 < 1$; this is a result of the fact that, with identical wall interaction energies, the identical interaction ranges entropically penalize the larger species more during adsorption. As pressure is increased, this effect continues to reduce the amount of the species 1 present in the pore. Figure 9 shows the structure of the two components in a rigid pore as the pressure increases. Both components adsorb primarily at the interface at low pressures before forming a more heterogeneous structure in the center of the pore at higher pressures. Along the $x_1 = 0.05$ isopleth, we observe that the larger species adsorbs primarily along the walls at low pressures, but as the pore is loaded it is progressively expelled to the interior owing to competition with the smaller species at the walls. When the larger species is in excess in the bulk, $x_1 = 0.75$, the structure of the two components changes qualitatively very little as the bulk pressure is increased. Once again, the fluid bridge forms after the "shoulder" in $S_{1,2}$ (cf. SM) leading to a contraction of the material which is relaxed once the pore has filled.

C. Weak/strong fluid-wall interactions with asymmetric ranges

Next we consider the consequences of increasing the interaction strength of each species with the walls independently, without changing the interaction ranges. Figure 10 depicts the adsorption and selectivity curves when $\epsilon_{2,w}$ has been increased from 2.50 to 5.00 ($\lambda_{1,w} = \lambda_{2,w} = 1.50$). In this "strong binding" limit, we observe the Langmuirian adsorption of the bulk fluid when $x_1 \geq 0.25$ (upper panel). However, for $x_1 = 0.05$, a weak jump occurs around $P^* \approx 0.10$. The jump is much weaker when the bulk fluid has a larger mole fraction of the larger species and is most noticeable when the large species is more dilute. This is associated with the change in the composition of

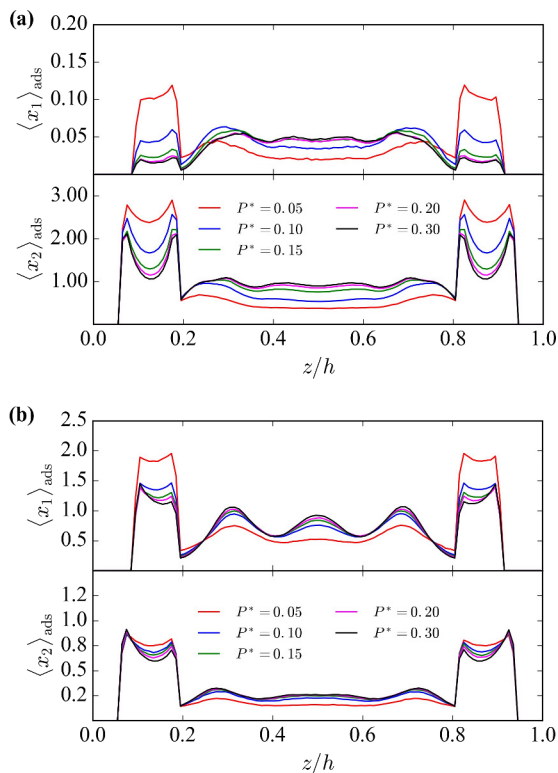


FIG. 9. Normalized ensemble-averaged density distribution of each species for $\epsilon_{1,w} = \epsilon_{2,w} = 2.50$, $\lambda_{1,w} = 1.00$, $\lambda_{2,w} = 1.50$. (a) Distribution throughout the pore for the isopleth $x_1 = 0.05$ for (top) species 1 and (bottom) species 2 at various pressures. (b) Distribution throughout the pore for the isopleth $x_1 = 0.75$ for (top) species 1 and (bottom) species 2 at various pressures. The pore width is fixed at $h = h_0 = 8\sigma_{2,2}$ and the pressures depicted correspond to those indicated in Fig. 8.

the pore, as evidenced by the selectivity curve (lower panel) simply because the larger species is being disproportionately displaced by the smaller one, allowing a larger number of molecules into the pore. Because of the strong wall interactions, the smaller species is much more prevalent in the pore at low pressure where $S_{1,2} \approx 0.27$. Once again, as the mole fraction of the larger species is decreased, the

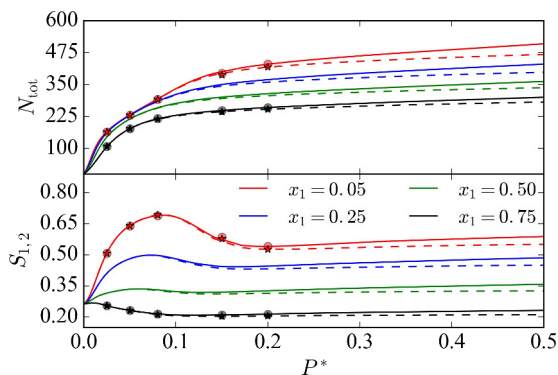


FIG. 10. (Top) Total number of molecules adsorbed in the slit pore for $\epsilon_{1,w} = 2.50$, $\epsilon_{2,w} = 5.00$, $\lambda_{1,w} = \lambda_{2,w} = 1.50$ when $K_T A = 500$ along representative isopleths. (Bottom) The corresponding selectivity for species 1 (large) relative to 2 (small). Solid lines correspond to the grand canonical pore ensemble, whereas dashed lines refer to the osmotic pore ensemble. Spheres and stars indicate the pressures at which rigid pore simulations were used to examine the fluid structure within the pore (cf. Fig. 11).

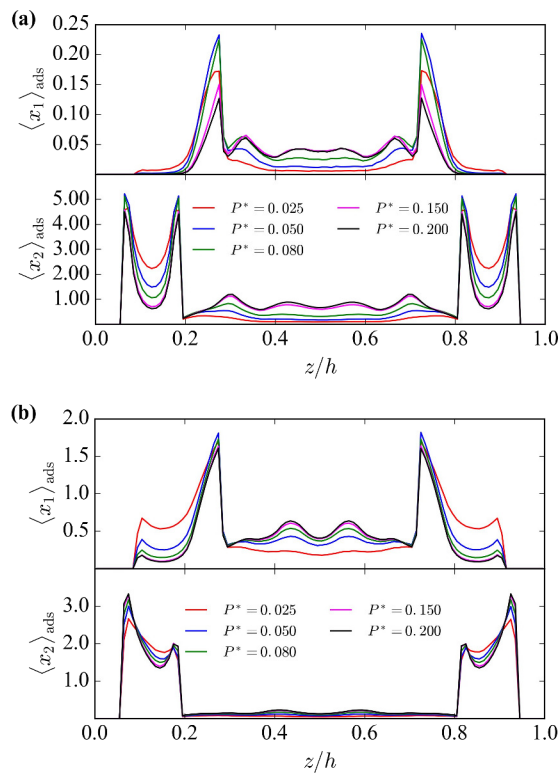


FIG. 11. Normalized ensemble-averaged density distribution of each species for $\epsilon_{1,w} = 2.50$, $\epsilon_{2,w} = 5.00$, $\lambda_{1,w} = \lambda_{2,w} = 1.50$. (a) Distribution throughout the pore for the isopleth $x_1 = 0.05$ for (top) species 1 and (bottom) species 2 at various pressures. (b) Distribution throughout the pore for the isopleth $x_1 = 0.75$ for (top) species 1 and (bottom) species 2 at various pressures. The pore width is fixed at $h = h_0 = 8\sigma_{2,2}$ and the pressures depicted correspond to those indicated in Fig. 10.

selectivity of the pore increases, adsorbing progressively more of the larger species up to $P^* \approx 0.10$. Figure 11 shows the structure of the two components inside the pore at the pressures indicated in Fig. 10. Again, for $x_1 = 0.05$ we observe that the smaller component adsorbs strongly at the wall forming a bilayer, creating a strongly adsorbing interface for the larger species. As for the case of $\epsilon_{2,w} = 2.50$, the larger species adsorbs atop this layer in a fashion which is non-monotonic in pressure, going through a maximum around $P^* \approx 0.10$. This corresponds to the point where $S_{1,2}$ reaches its local maximum and begins to decay as pore filling (entropic) effects displace the larger species in favor of the smaller one, thereby reducing $S_{1,2}$. When $x_1 = 0.75$, the strong wall interaction with the smaller species implies that this species still forms a bilayer even when it is not in great excess, unlike when its interaction was weaker, in which case composition controls which species adsorbs at the boundary. As a result, the larger species still forms an additional layer atop this bilayer of the smaller component even though its normalized density (height of the peak in the upper panel of Fig. 11(b)) is essentially invariant to increases in pressure. The fluid-fluid interactions in this case are insufficient to draw the adsorbed layer of larger species into the pore's interior as the fluid bridge forms because this fluid, largely similar to the bulk composition, is also primarily composed of this species. Therefore, the average number of contacts a molecule of the larger species can make in the interior of the channel is less

than that made at the interface of the bilayer, implying the latter remains a very stable adsorption location. Again, the formation of a fluid bridge marks the end of the non-monotonic behavior of $S_{1,2}$, which results in pore contraction at low to intermediate pressures. As pressure increases further, changes in the average pore width commensurate with the trends in Fig. 6 again manifest themselves. In the osmotic pore ensemble, pore filling leads to uniform expansion at pressures well above the point where $S_{1,2}$ goes through its maximum, whereas in the grand canonical pore ensemble, the oscillations in $\langle h \rangle / h_0$ associated with the formation of layers have a larger amplitude than those observed when $\epsilon_{2,w}$ is smaller (cf. SM).

D. Strong/weak fluid-wall interactions with asymmetric ranges

Finally, we consider the instance where the larger species is more strongly interacting with the wall ($\epsilon_{1,w} = 5.00$) than the smaller species ($\epsilon_{2,w} = 2.50$) for the same set of interaction ranges. The corresponding adsorption isotherms and structures are shown in Figs. 12 and 13, respectively. The larger species is favored, $S_{1,2} > 1$, for all isopleths although the magnitude of this preference quickly decays as the pore fills owing to packing considerations. Although weak, for bulk fluids where the larger species is the minor component ($x_1 = 0.05$), the selectivity again exhibits an initial rise before decaying. Figure 13 depicts the structure of the fluid along the $x_1 = 0.05, 0.75$ isopleths as pressure is increased, at the points indicated in Fig. 12. Although the larger species is energetically more favored at the wall, when it is dilute ($x_1 = 0.05$) the smaller species is entropically favored at the wall and again forms a bilayer, despite its weaker energetic interaction. Once more, the larger species primarily adsorbs in an adjacent layer, where the amount in the layer is a non-monotonic function of pressure. Even in this case, there is a corresponding weak non-monotonic behavior of $S_{1,2}$ as pressure increases. For a bulk fluid where $x_1 = 0.75$ the large species dominates at the interface with the wall,

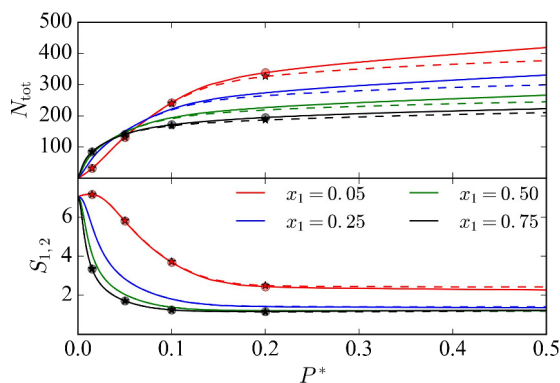


FIG. 12. (Top) Total number of molecules adsorbed in the slit pore for $\epsilon_{1,w} = 5.00$, $\epsilon_{2,w} = 2.50$, $\lambda_{1,w} = \lambda_{2,w} = 1.50$ when $K_T A = 500$ along representative isopleths. (Bottom) The corresponding selectivity for species 1 (large) relative to 2 (small). Solid lines correspond to the grand canonical pore ensemble, whereas dashed lines refer to the osmotic pore ensemble. Spheres and stars indicate the pressures at which rigid pore simulations were used to examine the fluid structure within the pore (cf. Fig. 13).

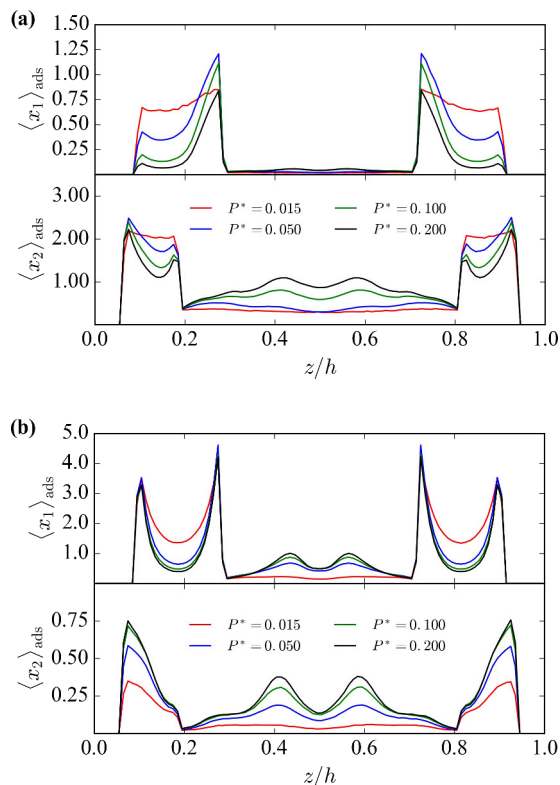


FIG. 13. Normalized ensemble-averaged density distribution of each species for $\epsilon_{1,w} = 5.00$, $\epsilon_{2,w} = 2.50$, $\lambda_{1,w} = \lambda_{2,w} = 1.50$. (a) Distribution throughout the pore for the isopleth $x_1 = 0.05$ for (top) species 1 and (bottom) species 2 at various pressures. (b) Distribution throughout the pore for the isopleth $x_1 = 0.75$ for (top) species 1 and (bottom) species 2 at various pressures. The pore width is fixed at $h = h_0 = 8\sigma_{2,2}$ and the pressures depicted correspond to those indicated in Fig. 12.

forming bilayers as in the case where $\epsilon_{1,w} = \epsilon_{2,w} = 2.50$. The smaller species still invades these layers, although it principally adsorbs directly at the wall as an additional layer competes with the second layer of the larger component for space.

IV. CONCLUSIONS AND OUTLOOK

We demonstrated a new simulation methodology for studying the adsorption of multicomponent fluids in flexible materials using flat-histogram Monte Carlo methods. This methodology produces the complete free energy landscape of the multicomponent mixture and permits us to easily investigate the behavior of the adsorbed fluid at arbitrary overall bulk compositions. Although we employed a simplified slit-pore model here, this methodology is fully extensible to realistic materials. The only requirement is that the free energy of the adsorbent be specified as a scalar function of pore size. We systematically investigated the consequences of changing the strength and interaction range of the adsorbent with each component, which are size asymmetric. The range, rather than the strength of any individual interaction, controls whether competitive or cooperative adsorption occurs at the walls of the slit pore. When the interaction ranges are symmetric, the species compete for adsorption sites at the walls and we recover conventional

competitive adsorption behavior between large and small species.

In all cases, where the interaction ranges between the walls and species are asymmetric, even after the pore has filled, the pore's selectivity for the larger species increases as its bulk mole fraction decreases. We attribute this to the inhomogeneous structure of the fluid in the pore. The non-monotonic behavior in $S_{1,2}$ for intermediate pressures at very low bulk x_1 is attributed to a balance between the cooperative adsorption enhancement the smaller species provides the larger one in adjacent layers, and the interactions the larger species has with the fluid in the interior of the pore. The latter becomes dominant as a fluid bridge forms between the opposite walls, reducing but not eliminating, the propensity of the larger species to adsorb on the bilayer of smaller species both energetically and entropically. This non-monotonicity terminates as the pore becomes filled, which is accompanied by a strain signature present in both flexible pore ensembles.

In the osmotic pore ensemble, the Hookean materials we studied here contract as the fluid bridge forms. In the grand canonical pore ensemble, the rate of the material's (internal) expansion with increasing bulk pressure is decreased. The subsequent expansion is a result of pore filling and further oscillations are the result of layers forming in the pore. We point out that the observed changes in the pore width are not related to capillary condensation since the temperature is supercritical for both species. However, we do expect this to play an important role at subcritical conditions, which will be subject of future contributions. This initial strain signature was still observed when such enhancement does not occur (cf. SM), as in the case when the total interaction ranges of the fluid's components with the walls are commensurate with each other ($\lambda_{1,w}\sigma_{1,1} = \lambda_{2,w}\sigma_{2,2}$). However, the termination of this initial mechanical strain provides a convenient macroscopic signature for the pressure at which non-monotonic selectivity enhancement is no longer even possible.

SUPPLEMENTARY MATERIAL

See the [supplementary material](#) for additional adsorption isotherms, a description of adsorbed fluid layering, and effects of different fluid-fluid interaction parameters.

ACKNOWLEDGMENTS

Contribution of the National Institute of Standards and Technology, not subject to US Copyright. N.A.M. gratefully acknowledges support from a National Research Council postdoctoral research associateship at the National Institute of Standards and Technology.

APPENDIX A: HISTOGRAM REWEIGHTING

Here we consider the partition functions in each of the relevant thermodynamic ensembles in order to obtain expressions for the probability of observing these systems in certain macrostates. We first consider the confined ternary system (binary adsorbate plus adsorbent) in a rigid pore at fixed h and h_p , adsorbate chemical potentials, μ_1 and μ_2 , temperature, $1/\beta$, and number of adsorbent atoms or molecules, N_s . The partition function describing the rigid pore can be written as

$$Z(\beta, Ah, \mu_1, \mu_2, N_s; h_p) = \sum_{N_1} \sum_{N_2} \exp(\beta\mu_1 N_1 + \beta\mu_2 N_2) \times Q(\beta, Ah, N_1, N_2, N_s), \quad (\text{A1})$$

where Q is the canonical partition function given by Eq. (7). Note that at fixed h , $Q_s(h)$ is just a constant which may be neglected such that $Q = Q_f$. In practice, we also neglect the momentum degrees of freedom (kinetic energy contribution) from the fluid in Q_f for simplicity, as they do not affect the extensive thermodynamic properties of the system. A change of variables where $\Delta\mu_2 \equiv \mu_2 - \mu_1$ allows this to be expressed as a sum over the total number of adsorbate molecules in the system, $N_{\text{tot}} = N_1 + N_2$.

$$Z(\beta, Ah, \mu_1, \mu_2, N_s; h_p) = \sum_{N_{\text{tot}}} \exp(\beta\mu_1 N_{\text{tot}}) \sum_{N_2} \exp(\beta\Delta\mu_2 N_2) Q_f(\beta, Ah, N_1, N_2, N_s), \quad (\text{A2})$$

$$Z(\beta, Ah, \mu_1, \mu_2, N_s; h_p) = \sum_{N_{\text{tot}}} \exp(\beta\mu_1 N_{\text{tot}}) \Upsilon(\beta, Ah, N_{\text{tot}}, \Delta\mu_2, N_s), \quad (\text{A3})$$

where $\Upsilon(\beta, Ah, N_{\text{tot}}, \Delta\mu_2, N_s)$ is the isochoric semigrand partition function.^{50,51} Note that this generalizes to any k -component system such that $\Upsilon(\beta, Ah, N_{\text{tot}}, \{\Delta\mu_2, \Delta\mu_3, \dots, \Delta\mu_k\}, N_s)$. Therefore, the probability, Π , of observing a macrostate of the system with N_{tot} molecules at fixed β , Ah , μ_1 , μ_2 , and N_s is

$$\Pi(N_{\text{tot}}; \mu_1) = \frac{\exp(\beta\mu_1 N_{\text{tot}}) \Upsilon(\beta, Ah, N_{\text{tot}}, \Delta\mu_2, N_s)}{Z(\beta, Ah, \mu_1, \mu_2, N_s)}. \quad (\text{A4})$$

Thus, the probability of observing such a macrostate under any imposed μ_1 can be calculated from a single probability distribution obtained at a reference μ_1^0 at the same β , V , $\Delta\mu_2$, and N_s using standard histogram reweighting techniques⁵²

$$\ln \Pi(N_{\text{tot}}; \mu_1) = \ln \Pi(N_{\text{tot}}; \mu_1^0) + \beta(\mu_1 - \mu_1^0) N_{\text{tot}} + C. \quad (\text{A5})$$

Here $C = \ln(Z(\mu_1^0)/Z(\mu_1))$, which in principle can be neglected as it is a constant and does not affect the

thermodynamic properties of the system. One of the principal advantages of this formalism is that the total number of molecules, N_{tot} , can be used as the lone order parameter in flat-histogram Monte Carlo simulations (cf. Appendix B).

In the grand canonical pore ensemble, h is allowed to fluctuate at fixed h_p (cf. Fig. 1). From Eq. (7), we can rewrite the canonical partition function for a pore with a fixed overall volume (h_p) as a sum over all possible values of h ,

$$\begin{aligned} Q(\beta, Ah_p, N_1, N_2, N_s) &= \sum_{h \leq h_p} Q_s(h) Q_f \\ &= \sum_{h \leq h_p} \exp(-\beta F_s(h)) Q_f. \end{aligned} \quad (\text{A6})$$

As a result, the probability of observing a macrostate of the system is now a function of the free energy profile of the solid, $F_s(h)$. Again, without loss of generality we have neglected the momentum degrees of freedom from Q_f . The grand canonical pore partition function can be expressed as

$$\Xi(\beta, Ah_p, \mu_1, \mu_2, N_s) = \sum_{h \leq h_p} \exp(-\beta F_s(h)) \sum_{N_{\text{tot}}} \exp(\beta \mu_1 N_{\text{tot}}) \sum_{N_2} \exp(\beta \Delta \mu_2 N_2) Q_f(\beta, Ah, N_1, N_2, N_s) \quad (\text{A7})$$

$$= \sum_{h \leq h_p} \exp(-\beta F_s(h)) \sum_{N_{\text{tot}}} \exp(\beta \mu_1 N_{\text{tot}}) \Upsilon(\beta, Ah, N_{\text{tot}}, \Delta \mu_2, N_s) \quad (\text{A8})$$

$$= \sum_{h \leq h_p} \exp(-\beta F_s(h)) Z(\beta, Ah, \mu_1, \mu_2, N_s; h_p). \quad (\text{A9})$$

In a similar fashion, the probability of observing a macrostate with a given h and N_{tot} is simply

$$\Pi_{\text{gc}}(h, N_{\text{tot}}) = \frac{\exp(-\beta F_s(h) + \beta \mu_1 N_{\text{tot}}) \Upsilon(\beta, Ah, N_{\text{tot}}, \Delta \mu_2, N_s)}{\Xi(\beta, Ah_p, \mu_1, \mu_2, N_s)}, \quad (\text{A10})$$

which implies that this can be calculated at any imposed μ_1 from any other known probability distribution obtained at the same β , A , h , h_p , $\Delta \mu_2$, and N_s ,

$$\ln \Pi_{\text{gc}}(h, N_{\text{tot}}; \mu_1) = \ln \Pi_{\text{gc}}(h, N_{\text{tot}}; \mu_1^0) + \beta(\mu_1 - \mu_1^0) N_{\text{tot}} + C, \quad (\text{A11})$$

where $C = \ln(\Xi(\mu_1^0)/\Xi(\mu_1))$, which once again may be neglected.

If we consider the osmotic pore ensemble, the results are very similar; only one additional Legendre transform is necessary to account for the fact that h_p can fluctuate. Since we take $h = h_p$ when working in this ensemble, the osmotic pore partition function may be simplified to

$$\Gamma(\beta, P, \mu_1, \mu_2, N_s) = \sum_{h_p} \exp(-\beta P A h_p) \sum_{h \leq h_p} \exp(-\beta F_s(h)) \sum_{N_{\text{tot}}} \exp(\beta \mu_1 N_{\text{tot}}) \quad (\text{A12})$$

$$\times \left[\sum_{N_2} \exp(\beta \Delta \mu_2 N_2) Q_f(\beta, Ah, N_1, N_2, N_s) \right] \quad (\text{A13})$$

$$= \sum_h \exp(-\beta P A h - \beta F_s(h)) \sum_{N_{\text{tot}}} \exp(\beta \mu_1 N_{\text{tot}}) \sum_{N_2} \exp(\beta \Delta \mu_2 N_2) Q_f(\beta, Ah, N_1, N_2, N_s) \quad (\text{A14})$$

$$= \sum_h \exp(-\beta P A h - \beta F_s(h)) \sum_{N_{\text{tot}}} \exp(\beta \mu_1 N_{\text{tot}}) \Upsilon(\beta, Ah, N_{\text{tot}}, \Delta \mu_2, N_s) \quad (\text{A15})$$

$$= \sum_h \exp(-\beta P A h - \beta F_s(h)) Z(\beta, Ah, \mu_1, \mu_2, N_s; h_p). \quad (\text{A16})$$

Therefore the probability of observing a macrostate with a given h and N_{tot} in the osmotic pore ensemble is given by

$$\Pi_{\text{os}}(h, N_{\text{tot}}) = \frac{\exp(-\beta F_s(h) - \beta P A h + \beta \mu_1 N_{\text{tot}}) \Upsilon(\beta, Ah, N_{\text{tot}}, \Delta \mu_2, N_s)}{\Gamma(\beta, P, \mu_1, \mu_2, N_s)}. \quad (\text{A17})$$

As in the grand canonical pore ensemble, the probability of observing a macrostate with a given h and N_{tot} at any imposed μ_1 can be found once the probability distribution has been calculated for some μ_1^0 ,

$$\ln \Pi_{\text{os}}(h, N_{\text{tot}}; \mu_1) = \ln \Pi_{\text{os}}(h, N_{\text{tot}}; \mu_1^0) + \beta(\mu_1 - \mu_1^0) N_{\text{tot}} - \beta A h (P - P^0) + C. \quad (\text{A18})$$

Once more, the additive constant is a ratio of partition functions, $C = \ln(\Gamma(\mu_1^0)/\Gamma(\mu_1))$, which is constant and is neglected in practice.

APPENDIX B: SIMULATION METHODOLOGY

We employed a computationally efficient flat-histogram Monte Carlo method known as Wang-Landau Transition Matrix Monte Carlo (WL-TMMC) to construct the macrostate probability distribution of our system composed of two species and a coarse-grained flexible adsorbent. This method has been described in more detail elsewhere,^{10,19,42,53,54} but we summarize our implementation here. Both the Wang-Landau and transition matrix methods are flat histogram methods, which seek to construct a biasing function with which the acceptance criteria of Monte Carlo moves are modified. We employed three types of moves: insertion and deletion of individual species, displacement of an individual species, and an identity swap which transmuted a molecule of species 1 into 2 or *vice versa*. These were attempted with a 2:1:1 ratio, respectively. All simulations were performed in a rectangular $10\sigma_{2,2} \times 10\sigma_{2,2} \times h_p$ cell. For bulk simulations, the cell was periodic in all dimensions and $h_p = 10\sigma_{2,2}$. For confined fluids, $h_p = 13\sigma_{2,2}$ and the slit-pore walls were placed symmetrically in the box a distance of h apart. These walls conferred non-periodicity in the z -direction.

The $\ln \Pi(h, N_{\text{tot}})$ surface for both pore ensembles was constructed by performing a series of rigid pore simulations which were exposed to a reservoir of adsorbate at fixed chemical potentials and temperature, i.e., the grand canonical ensemble (not to be confused with the grand canonical pore ensemble). For a rigid pore (fixed h_p and h), the unbiased move acceptance criteria are related to the ratio of the probabilities of observing the final and initial microstates. The probability of observing a configurational microstate, s , in this ensemble is given by

$$\pi(s) = \frac{\exp(-\beta U(s))}{Z} \prod_{i=1}^2 \frac{V^{N_i(s)} \exp(\beta \mu_i N_i(s))}{N_i(s)!}, \quad (\text{B1})$$

where Z is given by Eq. (A1) and $U(s)$ is the potential energy of the microstate. Thus, the unbiased Metropolis acceptance criteria of moving from microstate “ a ” to “ b ” is

$$p_u = \min \left[1, \frac{\pi(b)}{\pi(a)} \right]. \quad (\text{B2})$$

A proposed move was accepted with a probability that was biased by some function, $\eta(N_{\text{tot}})$, which depended on the order parameter we selected, $N_{\text{tot}} = N_1 + N_2$,

$$p_{\text{bias}} = \min \left[1, \frac{\exp(\eta[N_{\text{tot}}(b)]) \pi(b)}{\exp(\eta[N_{\text{tot}}(a)]) \pi(a)} \right]. \quad (\text{B3})$$

Our objective was to sample the N_{tot} space evenly in order to leverage histogram reweighting techniques as described in Appendix A, and thus, the ideal biasing function is given by

$$\eta(N_{\text{tot}}) = -\ln \Pi(N_{\text{tot}}). \quad (\text{B4})$$

For each rigid pore, we iteratively constructed η using Wang-Landau simulations initially, which were then refined

by transition matrix methods. Once η had sufficiently converged, Eq. (B4) provided $\ln \Pi(N_{\text{tot}})$. An empty system was initialized at the beginning of a simulation and Monte Carlo moves were continuously performed. The biasing function’s estimate of the macrostate probability distribution, $\ln \Pi(N_{\text{tot}})$, was initialized to zero for all N_{tot} permissible. After a trial move was proposed, this estimate was continuously updated

$$\ln \Pi(N_{\text{tot}}) = \ln \Pi(N_{\text{tot}}) + \ln f, \quad (\text{B5})$$

where $\ln f$ is the update factor and N_{tot} refers to the total number of molecules in the system after the move has been attempted, regardless of its success. Initially $\ln f = 1$, but was progressively reduced as the simulation converged. Convergence was estimated by recording a histogram, $H(N_{\text{tot}})$, of the frequency at which each macrostate was visited

$$H(N_{\text{tot}}) = H(N_{\text{tot}}) + 1, \quad (\text{B6})$$

where again N_{tot} refers to the total number of molecules in the system after a move was attempted. Since the biasing function should be the inverse of the probability of observing a state during unbiased sampling, all states should be visited with equal probability when the ideal biasing function has been applied. The degree to which Eq. (B4) approximates this ideal function is captured by the flatness of the visited-states histogram. We employed the common criterion where the minimum of $H(N_{\text{tot}})$ must be within 80% of the mean value

$$\min [H(N_{\text{tot}})] = 0.8 \langle H(N_{\text{tot}}) \rangle. \quad (\text{B7})$$

This condition was checked periodically and once satisfied, $H(N_{\text{tot}})$ was reset to zero and $\ln f$ was reduced by a factor of 2. This was repeated until $\ln f$ became appreciably small, usually around 27 times ($\ln f < 10^{-8}$) or more. The Wang-Landau algorithm builds a reasonable estimate of $\ln \Pi$ through Eq. (B5) quickly but tends to converge slowly as the update factor becomes smaller and smaller. To overcome this, Transition Matrix Monte Carlo (TMMC) was employed after this initial Wang-Landau stage.

A TMMC simulation also provides an estimate of $\ln \Pi$ for Eq. (B4) but does so by considering the transition rates between neighboring macrostates. This is stored in the collection matrix, C , which accumulates statistics about the unbiased probability of moving between two macrostates “ a ” and “ b ,” i.e., $N_{\text{tot}}(a) \rightarrow N_{\text{tot}}(b)$. Such a simulation proceeds by using the biased acceptance criterion in Eq. (B3) but accumulates the unbiased probability (cf. Eq. (B2)) measured for an attempted move

$$C[N_{\text{tot}}(a) \rightarrow N_{\text{tot}}(b)] = C[N_{\text{tot}}(a) \rightarrow N_{\text{tot}}(b)] + p_u, \quad (\text{B8})$$

$$C[N_{\text{tot}}(a) \rightarrow N_{\text{tot}}(a)] = C[N_{\text{tot}}(a) \rightarrow N_{\text{tot}}(a)] + 1 - p_u. \quad (\text{B9})$$

This scheme updates entries in the collection matrix associated with acceptance and rejection of the move, regardless of whether the move is actually accepted or not. Note that when a move is performed which does not change the order parameter N_{tot} , such as a displacement or identity swap, $N_{\text{tot}}(a) = N_{\text{tot}}(b)$, which results in $C[N_{\text{tot}}(a)]$ being updated by unity. The transition probability, $P[a \rightarrow b]$, of going from macrostate “ a ” to “ b ” is computed by normalizing

the accumulated unbiased probabilities of this transition over all possible transitions which begin in macrostate “*a*,”

$$P[a \rightarrow b] = \frac{C [N_{\text{tot}}(a) \rightarrow N_{\text{tot}}(b)]}{\sum_k C [N_{\text{tot}}(a) \rightarrow N_{\text{tot}}(k)]}. \quad (\text{B10})$$

Because we only proposed Monte Carlo moves which changed the order parameter N_{tot} at most by unity, C and P were triple-banded sparse matrices. Microscopic reversibility (detailed balance condition) implies that the macrostate distribution can be directly computed from the probability matrix

$$\ln \Pi(N_{\text{tot}} + 1) = \ln \Pi(N_{\text{tot}}) + \frac{P [N_{\text{tot}} \rightarrow N_{\text{tot}} + 1]}{P [N_{\text{tot}} + 1 \rightarrow N_{\text{tot}}]}. \quad (\text{B11})$$

The value for $\ln \Pi(0)$ was set to zero to allow the rest of the distribution to be calculated incrementally; however, this value is irrelevant since the distribution was later normalized. The bias function which was constructed from the initial Wang-Landau portion of the simulation was still used for a period while the collection matrix was initially being constructed. After which the simulation discarded this information and used the collection matrix to compute its bias function.

During the TMMC portion of the simulation, sweeps of moves were performed after which the biasing function was recomputed before the next cycle. A sweep was defined to be the number of steps required for a simulation to sample each position in the collection matrix at least 5 times when p_u was finite. Thus, the number of steps required depends on the interactions in the system, the mix of Monte Carlo moves employed, and the system density. However, requiring a minimum number of passes in the collection matrix balances this across different scenarios and improved convergence. Because the collection matrix is updated with p_u , which is always less than or equal to unity, the matrix builds up very slowly if started from a poor initial guess, but converges quickly once it becomes more accurate. The Wang-Landau portion provides this initial guess which greatly accelerates the convergence of the collection matrix. Once a sufficient number of sweeps were performed, the converged bias function provided the macrostate probability distribution via Eq. (B4). Typically 10^3 sweeps during the TMMC portion of the simulation were required to converge simulations, which amounted to roughly 10^9 Monte Carlo steps depending on the factors mentioned above.

APPENDIX C: ISOPLETH REFINEMENT

The initial estimate of the isopleth (μ_1, μ_2) parameterization for a bulk fluid described in Sec. II C 2 can be refined by performing a local optimization at discrete points along the estimated isopleth as follows. For each point $(\mu_1^i, \Delta\mu_2^i)$ along the isopleth, the macrostate probability distribution function at $\Delta\mu_2^i$ may be estimated by linearly interpolating the distribution from its neighbors at $\Delta\mu_2^a$ and $\Delta\mu_2^b$, where $\Delta\mu_2^a < \Delta\mu_2^i < \Delta\mu_2^b$. This distribution at $(\mu_1^i, \Delta\mu_2^i)$ may be subsequently reweighted to $(\mu_1^i, \Delta\mu_2^i)$ and Eq. (16) used to assess the accuracy of this initial parameterization. Usually we found that this initial estimate deviated at most 5% from

the desired x_1 ; however, locally optimizing μ_1 easily improved this error to 0.1% or less. The optimized parameterization was employed throughout this study.

APPENDIX D: GENERATING THE PROBABILITY SURFACE

The objective of flat histogram simulation methods is to obtain a bias which permits the simulation to walk in an effectively random fashion throughout the phase space set by the order parameter of the bias. Even in the case when the ideal bias function has been obtained, traversing large distances can take a great deal of time since the number of steps required to traverse the distance between two macrostates should scale as the square of distance between them. Therefore it is often much more efficient to divide the phase space into “windows” where each window, k , has some predefined bounds $N_{\text{tot},\text{min}}^k \leq N_{\text{tot}}^k \leq N_{\text{tot},\text{max}}^k$.

All calculations began with a series of rigid pore grand canonical simulations. Each set in the series was composed of approximately 15 windows with varying ranges of N_{tot} they each sampled, all at the same fixed $\Delta\mu_2$ and $\mu_1^0 = 0$, though the exact value of μ_1^0 is irrelevant. Windows at low density typically had a width of approximately 100 total molecules, which was scaled by a power law down to as little as 12 total molecules at the highest densities sampled. Each window shared at least 4 common N_{tot} with its nearest neighboring windows whose widths were chosen to prevent any overlap between three or more such windows. The endpoints of each distribution were excluded from this overlap. A composite $\ln \Pi(N_{\text{tot}})$ was constructed by taking one window initially as a reference state, then minimizing the error between the estimates of $\ln \Pi(N_{\text{tot}})$ in the overlapping region between windows “*a*” and “*b*,”

$$\chi^2 = \sum_{N_{\text{tot}} \in a \cap b} (\ln \Pi_a(N_{\text{tot}}) - (\ln \Pi_b(N_{\text{tot}}) + C))^2. \quad (\text{D1})$$

Minimization of χ^2 for each overlap yields a constant shift C for, in this case, distribution “*b*.” In all cases, only overlapping windows with a χ^2 corresponding to less than a 1% systematic error in $\Pi(N_{\text{tot}})$ were accepted as valid. The entire window distribution $\ln \Pi_b(N_{\text{tot}})$ was then shifted by C , then the two windows were merged. At each N_{tot} , properties such as U , N_1 , and N_2 were measured. In the overlapping region, the values for the composite histogram were estimated from their contributing windows by a weighted average of the two contributing histograms to smooth the overlap. However, simulations were run long enough to ensure that overlapping windows produced estimates of the extensive properties at the same N_{tot} within a few percent so this smoothing was relatively inconsequential. On an Intel Xeon 2.4 GHz processor, a window typically reached this level of convergence in less than 48 wallclock hours. This process was iteratively repeated to construct the complete $\ln \Pi(N_{\text{tot}})$ distribution over all k windows.

Additional sets of simulations were performed at intervals of $\Delta\mu_2$ (typically $\delta(\Delta\mu_2) = 0.5$), all with the same μ_1 , to build a grid as shown in Fig. 3 which spans a range of mole fractions

as desired. During rigid pore grand canonical simulations in which the move acceptance criteria are given by Eq. (B2), the ideal gas reference state is obtained as $\mu_i \rightarrow -\infty$. From Eq. (B1), it is clear that one indeed recovers, $\beta\mu_i = \ln(N_i/V)$. The construction of the (μ_1, μ_2) surface requires knowledge of the range of $\Delta\mu_2 = \mu_2 - \mu_1$, over which to sample. Given a target set of mole fractions (isopleths) we would like to investigate, an initial guess on the bounds to sample may be obtained from simple algebra

$$\exp(\beta\mu_1) = N_1/V, \quad (D2)$$

$$\exp(\beta\mu_2) = \exp(\beta(\mu_1 + \Delta\mu_2)) = N_2/V. \quad (D3)$$

It follows that the mole fraction of species 1 in the dilute limit may be expressed as

$$x_1 = \frac{\exp(\beta\mu_1)}{\exp(\beta\mu_1) + \exp(\beta(\mu_1 + \Delta\mu_2))}, \quad (D4)$$

which may be rearranged to

$$\ln(1/x_1 - 1) = \beta\Delta\mu_2. \quad (D5)$$

Therefore, given a bounded range of target isopleths ($x_{1,\min} \leq x_1 \leq x_{1,\max}$), a range of $\Delta\mu_{2,\min} \leq \Delta\mu_2 \leq \Delta\mu_{2,\max}$ can also be estimated. As density increases out of the ideal gas limit (μ_1 at a given $\Delta\mu_2$), the isopleths will begin to deviate from a line of constant $\Delta\mu_2$ and potentially move outside the initially estimated range. Thus, this initial range of $\Delta\mu_2$'s can be simulated to observe the behavior of the gas as the density begins to increase, then progressively expanded as necessary (cf. Fig. 3).

Once a sufficiently wide grid has been constructed, an arbitrary macrostate distribution at a given $(\mu_1^0, \Delta\mu_2)$ may be estimated by linearly interpolating between neighboring distributions. First, for a target set of conditions (μ_1^t, μ_2^t) , we ensured $\Delta\mu_2^t = \mu_2^t - \mu_1^t$ was within the bounds of the grid simulated. Then, we obtained $\ln \Pi(N_{\text{tot}})$ at $(\mu_1^0, \Delta\mu_2^t)$ by linearly interpolating from its nearest bounding neighbors in the grid, $\Delta\mu_2^a < \Delta\mu_2^t < \Delta\mu_2^b$,

$$\ln \hat{\Pi}(N_{\text{tot}}; \Delta\mu_2^t) = \xi (\ln \Pi_b(N_{\text{tot}}) - \ln \Pi_a(N_{\text{tot}})) + \ln \Pi_a(N_{\text{tot}}), \quad (D6)$$

where $\xi = (\Delta\mu_2^t - \Delta\mu_2^a)/(\Delta\mu_2^b - \Delta\mu_2^a)$. This distribution was subsequently reweighted from μ_1^0 to μ_1^t using Eq. (A5) to obtain $\ln \Pi(N_{\text{tot}}; \mu_1^t, \mu_2^t)$. This linear interpolation scheme was also used to estimate the ensemble-averaged extensive properties at each N_{tot} . For calculations involving bulk systems, such as to obtain the isopleths in Fig. 3, this is sufficient. However, for confined systems, this same series containing a grid of $\Delta\mu_2$ values must be repeated for each value of h . Thus, for each h value we obtained a grid such as depicted in Fig. 3 from which we interpolated $\ln \Pi(h, N_{\text{tot}})$ over the desired range of chemical potentials (μ_1, μ_2) defined along the isopleths obtained from bulk simulations. We simulated a set of h values such that $6\sigma_{2,2} \leq h \leq 10\sigma_{2,2}$ at intervals of $\delta h = 0.5\sigma_{2,2}$. This grid was also refined via linear interpolation down to $\delta h = 0.025\sigma_{2,2}$ by interpolating the macrostate distributions at each $\Delta\mu_2$ in the grid between neighboring values of h , i.e., Eq. (D6) was repeated using $\xi = (h^t - h^a)/(h^b - h^a)$.

At a given (μ_1, μ_2) , the rigid pore simulations must be combined in order to produce a probability distribution for a flexible material in either the grand canonical pore or osmotic pore ensemble. By examining the thermodynamic expressions derived in Appendix A, it is clear how this may be achieved in the limit of $N_{\text{tot}} = 0$. In this pure adsorbent limit Eqs. (A10) and (A17) become, respectively,

$$\ln \Pi_{\text{gc}}(h, 0) = -\beta F_s(h) + C_{\text{gc}}, \quad (D7)$$

$$\ln \Pi_{\text{os}}(h, 0) = -\beta F_s(h) - \beta P(\beta, \mu_1, \mu_2)Ah + C_{\text{os}}, \quad (D8)$$

where C_{gc} and C_{os} are constants related to the partition functions of each ensemble. We chose to set them to zero and shift the entire rigid pore macrostate distributions at each h , for a given (μ_1, μ_2) , such that these expressions correctly describe $\ln \Pi(h, N_{\text{tot}})$ in the pure adsorbent limit. Here we have written the pressure for the osmotic pore ensemble as a function of the temperature and chemical potentials to emphasize that this is a function of the bulk adsorbate reservoir conditions at each state point considered. The result is a three dimensional surface of $\ln \Pi(h, N_{\text{tot}})$ as depicted in Fig. 4.

APPENDIX E: BULK FLUID PHASE BEHAVIOR

The fluid phase behavior of each pure component, i , was obtained in a periodic cubic simulation box with each box dimension $L = 9\sigma_{i,i}$ ($V = L^3$), at various subcritical temperatures using these flat-histogram methods. By analogy to Eqs. (A4) and (A5) for a pure component system, we have

$$\Pi(N_i; \mu_i) = \frac{\exp(\beta\mu_i N_i) Q_{\text{pure}}(\beta, V, N_i)}{\Xi(\beta, V, \mu_i)}, \quad (E1)$$

$$\ln \Pi(N_i; \mu_i) = \ln \Pi(N_i; \mu_i^0) + \beta(\mu_i - \mu_i^0)N_i. \quad (E2)$$

For each temperature, the macrostate distribution was reweighted to different μ_i values in an attempt to locate a bimodal distribution of $\ln \Pi(N_{\text{tot}})$ (cf. Fig. 14(b)). This curve was segmented into two regions based on the local minima between peaks, which defines the liquid and vapor phases. A Maxwell construction was then used to compute the binodal curve. Equilibrium is defined by the chemical potential where the (logarithm of the) sum of the probabilities of observing each macrostate belonging to each phase is equal. Results are depicted in Fig. 14,

$$\ln \left(\sum_{N_{\text{tot}} \in \text{vap}} \Pi(N_{\text{tot}}) \right) = \ln \left(\sum_{N_{\text{tot}} \in \text{liq}} \Pi(N_{\text{tot}}) \right). \quad (E3)$$

The law of rectilinear diameters was used to estimate the critical conditions for each component. For component 1, we found the critical point at $k_B T_{c,1}/\epsilon_{2,2} = 1.096 \pm 0.003$ and $N_c \sigma_{1,1}^3/V = 0.360 \pm 0.001$, where the uncertainty is the standard error from fitting the rectilinear scaling laws to the data⁵⁵

$$\frac{\rho_{\text{liq}} + \rho_{\text{vap}}}{2} = \rho_c + \hat{A}(T_c - T), \quad (E4)$$

$$\rho_{\text{liq}} - \rho_{\text{vap}} \sim (T_c - T)^{\hat{\beta}}, \quad (E5)$$

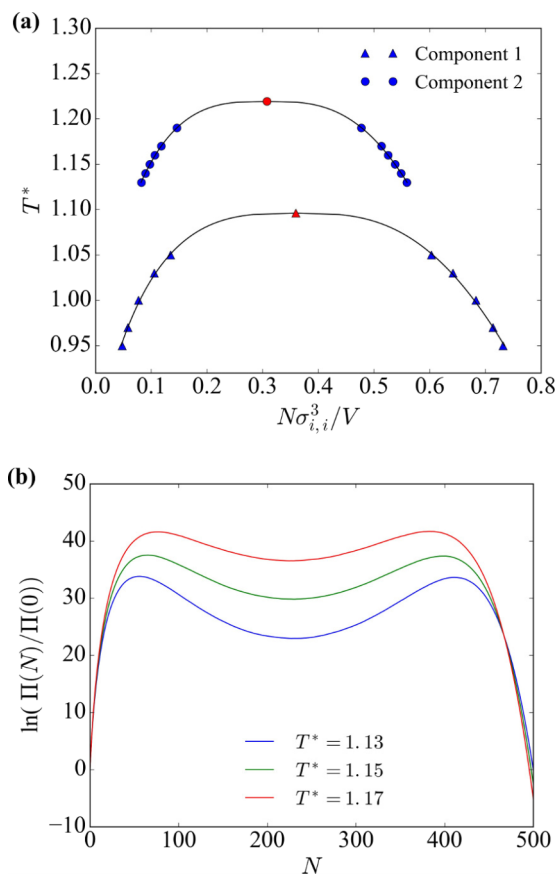


FIG. 14. (a) Pure component vapor-liquid binodals for both components used in this work. The density is reported in reduced units where the volume has been normalized by the diameter of each species; for component 1, $\sigma_{1,1} = 1.50$, and for component 2, $\sigma_{2,2} = 1.0$. Binodal points are shown in blue, the estimated critical point is shown in red, while the black lines are the fitted results from the law of rectilinear diameters. (b) Equilibrium macrostate probability distribution for component 2 along its binodal at each temperature indicated.

where $\hat{\beta} = 0.3258$ in three dimensions and \hat{A} is some fitting constant. For component 2, we obtained $k_B T_{c,2}/\epsilon_{2,2} = 1.219 \pm 0.001$ and $N_c \sigma_{2,2}^3/V = 0.308 \pm 0.001$.

The phase behavior of a bulk binary mixture can be calculated in a similar way. Grand canonical Monte Carlo simulations were used to produce a macrostate distribution following Eq. (A4) at a fixed $\Delta\mu_2$, where the volume was defined by the simulation box in the absence of any walls. For each $\Delta\mu_2$, the macrostate distribution was reweighted via Eq. (A5) to different μ_1 and a similar process was repeated to produce Fig. 2.

¹D. Britt, H. Furukawa, B. Wang, T. G. Glover, and O. M. Yaghi, "Highly efficient separation of carbon dioxide by a metal-organic framework replete with open metal sites," *Proc. Natl. Acad. Sci. U. S. A.* **106**, 20637–20640 (2009).

²J. A. Mason, J. Oktawiec, T. K. Mercedes, M. R. Hudson, J. Rodriguez, J. E. Bachman, M. I. Gonzalez, A. Cervellino, A. Guagliardi, C. M. Brown, P. L. Llewellyn, N. Masciocchi, and J. R. Long, "Methane storage in flexible metal-organic frameworks with intrinsic thermal management," *Nature* **527**, 357–361 (2015).

³D. I. Fried, F. J. Brieler, and M. Fröba, "Designing inorganic porous materials for enzyme adsorption and applications in biocatalysis," *ChemCatChem* **5**, 862–884 (2013).

⁴P. Horcajada, C. Serre, G. Maurin, N. A. Ramsahye, F. Balas, M. Vallet-Regí, M. Sebban, F. Taulelle, and G. Férey, "Flexible porous metal-organic

frameworks for a controlled drug delivery," *J. Am. Chem. Soc.* **130**, 6774–6780 (2008).

⁵W. J. Koros and R. P. Lively, "Water and beyond: Expanding the spectrum of large-scale energy efficient separation processes," *AIChE J.* **58**, 2624–2633 (2012).

⁶D. S. Sholl and R. P. Lively, "Seven chemical separations to change the world," *Nature* **532**, 435–437 (2016).

⁷R. J. Giraud, P. A. Williams, A. Sehgal, E. Ponnusamy, A. K. Phillips, and J. B. Manley, "Implementing green chemistry in chemical manufacturing: A survey report," *ACS Sustainable Chem. Eng.* **2**, 2237–2242 (2014).

⁸R. Evans, *Density Functionals in the Theory of Nonuniform Fluids* (Marcel Dekker, New York, 1992), Vol. 1.

⁹J. Landers, G. Y. Gor, and A. V. Neimark, "Density functional theory methods for characterization of porous materials," *Colloids Surf., A* **437**, 3–32 (2013).

¹⁰D. W. Siderius and V. K. Shen, "Use of the grand canonical transition-matrix Monte Carlo method to model gas adsorption in porous materials," *J. Phys. Chem. C* **117**, 5861–5872 (2013).

¹¹P. A. Monson, "The properties of inhomogeneous square-well mixtures in one dimension," *Mol. Phys.* **70**, 401–423 (1990).

¹²Z. Tan and K. E. Gubbins, "Selective adsorption of simple mixtures in slit pores: A model of methan-ethane mixtures in carbon," *J. Phys. Chem.* **96**, 845–854 (1992).

¹³R. F. Cracknell, D. Nicholson, and N. Quirke, "A grand canonical Monte Carlo study of Lennard-Jones mixtures in slit shaped pores," *Mol. Phys.* **80**, 885–897 (1993).

¹⁴P. B. Balbuena and K. E. Gubbins, "Theoretical interpretation of adsorption behavior of simple fluids in slit pores," *Langmuir* **9**, 1801–1814 (1993).

¹⁵J. Talbot, "Molecular thermodynamics of binary mixture adsorption: A scaled particle theory approach," *J. Chem. Phys.* **106**, 4696–4706 (1997).

¹⁶J. Talbot, "Analysis of adsorption selectivity in a one-dimensional model system," *AIChE J.* **43**, 2471–2478 (1997).

¹⁷S. Jana, J. K. Singh, and S. Kyu Kwak, "Vapor-liquid critical and interfacial properties of square-well fluids in slit pores," *J. Chem. Phys.* **130**, 214707 (2009).

¹⁸N. F. Cessford, N. A. Seaton, and T. Düren, "Evaluation of ideal adsorbed solution theory as a tool for the design of metal-organic framework materials," *Ind. Eng. Chem. Res.* **51**, 4911–4921 (2012).

¹⁹V. K. Shen and D. W. Siderius, "Elucidating the effects of adsorbent flexibility on fluid adsorption using simple models and flat-histogram sampling methods," *J. Chem. Phys.* **140**, 244106 (2014).

²⁰A. L. Myers and J. M. Prausnitz, "Thermodynamics of mixed-gas adsorption," *AIChE J.* **11**, 121–127 (1965).

²¹W. M. Jacobs and D. Frenkel, "Predicting phase behavior in multicomponent mixtures," *J. Chem. Phys.* **139**, 024108 (2013).

²²E. A. Ustinov and D. D. Do, "Effect of adsorption deformation on thermodynamic characteristics of a fluid in slit pore at sub-critical conditions," *Carbon* **44**, 2652–2663 (2006).

²³P. Kowalczyk, A. Ciach, and A. V. Neimark, "Adsorption-induced deformations of microporous carbons: Pore size and distribution effect," *Langmuir* **24**, 6603–6608 (2008).

²⁴T. J. H. Vlucht and M. Schenk, "Influence of framework flexibility on the adsorption properties of hydrocarbons in the zeolite silicalite," *J. Phys. Chem. B* **106**, 12757–12763 (2002).

²⁵G. Y. Gor, O. Paris, J. Prass, P. A. Russo, M. M. L. R. Carrott, and A. V. Neimark, "Adsorption of n-pentane on mesoporous silica and adsorbent deformation," *Langmuir* **29**, 8601–8608 (2013).

²⁶G. Y. Gor and N. Bernstein, "Adsorption-induced surface stresses of the water/quartz interface: *Ab initio* molecular dynamics study," *Langmuir* **32**, 5259 (2016).

²⁷A. V. Neimark, F.-X. Coudert, C. Triguero, A. Boutin, A. H. Fuchs, I. Beurroies, and R. Denoyel, "Structural transitions in MIL-53 (Cr): View from the outside and inside," *Langmuir* **27**, 4734–4741 (2011).

²⁸D. Fairen-Jimenez, S. A. Moggach, M. T. Wharmby, P. A. Wright, S. Parsons, and T. Düren, "Opening the gate: Framework flexibility in ZIF-8 explored by experiments and simulations," *J. Am. Chem. Soc.* **133**, 8900–8902 (2011).

²⁹F.-X. Coudert, A. Boutin, A. H. Fuchs, and A. V. Neimark, "Adsorption deformation and structural transitions in metal-organic frameworks: From the unit cell to the crystal," *J. Phys. Chem. Lett.* **4**, 3198–3205 (2013).

- ³⁰L. Zhang, G. Wu, and J. Jiang, "Adsorption and diffusion of CO₂ and CH₄ in zeolitic imidazolate framework-8: Effect of structural flexibility," *J. Phys. Chem. C* **118**, 8788–8794 (2014).
- ³¹F.-X. Coudert, "The osmotic framework adsorbed solution theory: Predicting mixture coadsorption in flexible materials," *Phys. Chem. Chem. Phys.* **12**, 10904–10913 (2010).
- ³²A. V. Neimark, F.-X. Coudert, A. Boutin, and A. H. Fuchs, "Stress-based model for the breathing of metal-organic frameworks," *J. Phys. Chem. Lett.* **1**, 445–449 (2010).
- ³³J. Zang, S. Nair, and D. S. Sholl, "Osmotic ensemble methods for predicting adsorption-induced structural transitions in nanoporous materials using molecular simulations," *J. Chem. Phys.* **134**, 184103 (2011).
- ³⁴D. Bousquet, F.-X. Coudert, and A. Boutin, "Free energy landscapes for the thermodynamic understanding of adsorption-induced deformations and structural transitions in porous materials," *J. Chem. Phys.* **137**, 044118 (2012).
- ³⁵D. Bousquet, F.-X. Coudert, A. G. J. Fossati, A. V. Neimark, and A. H. Fuchs, "Adsorption induced transitions in soft porous crystals: An osmotic potential approach to multistability and intermediate structures," *J. Chem. Phys.* **138**, 174706 (2013).
- ³⁶A. U. Ortiz, M.-A. Springuel-Huet, F.-X. Coudert, A. H. Fuchs, and A. Boutin, "Predicting mixture coadsorption in soft porous crystals: Experimental and theoretical study of CO₂/CH₄ in MIL-53(Al)," *Langmuir* **28**, 494–498 (2012).
- ³⁷A. Ghysels, L. Vanduyfhuys, M. Vandichel, and M. Waroquier, "On the thermodynamics of framework breathing: A free energy model for gas adsorption in mil-53," *J. Phys. Chem. C* **117**, 11540–11554 (2013).
- ³⁸L. Sun, J. T. Hirvi, T. Schatz, S. Kasa, and T. A. Pakkanen, "Estimation of montmorillonite swelling pressure: A molecular dynamics approach," *J. Phys. Chem. C* **119**, 19863–19868 (2015).
- ³⁹J. Zang, S. Chempath, S. Konduri, S. Nair, and D. S. Sholl, "Flexibility of ordered surface hydroxyls influences the adsorption of molecules in single-walled aluminosilicate nanotubes," *J. Phys. Chem. Lett.* **1**, 1235–1240 (2010).
- ⁴⁰L. Zhang, Z. Hu, and J. Jiang, "Sorption-induced structural transitions of zeolitic imidazolate framework-8: A hybrid molecular simulation study," *J. Am. Chem. Soc.* **135**, 3722–3728 (2013).
- ⁴¹J. R. Errington and V. K. Shen, "Direct evaluation of multicomponent phase equilibria using flat-histogram methods," *J. Chem. Phys.* **123**, 164103 (2005).
- ⁴²V. K. Shen and J. R. Errington, "Determination of fluid-phase behavior using transition matrix Monte Carlo: Binary Lennard-Jones mixtures," *J. Chem. Phys.* **122**, 064508 (2005).
- ⁴³W. A. Steele, "The physical interaction of gases with crystalline solids: I. Gas-solid energies and properties of isolated adsorbed atoms," *Surf. Sci.* **36**, 317–352 (1973).
- ⁴⁴N. A. Ockwig, O. Delgado-Friedrichs, M. O'Keefe, and O. M. Yaghi, "Reticular chemistry: Occurrence and taxonomy of nets and grammar for the design of frameworks," *Acc. Chem. Res.* **38**, 176–182 (2005).
- ⁴⁵H. Furukawa, K. E. Cordova, M. O'Keefe, and O. M. Yaghi, "The chemistry and applications of metal-organic frameworks," *Science* **341**, 123044 (2013).
- ⁴⁶W. L. McCabe and E. W. Thiele, "Graphical design of fractionating columns," *Ind. Eng. Chem.* **17**(6), 605–611 (1925).
- ⁴⁷D. Morineau, Y. Xia, and C. Alba-Simionesco, "Finite-size and surface effects on the glass transition of liquid toluene confined in cylindrical mesopores," *J. Chem. Phys.* **117**, 8966–8972 (2002).
- ⁴⁸A. R. A. Hamid, R. Mhanna, R. Lefort, A. Ghoufi, C. Alba-Simionesco, B. Frick, and D. Morineau, "Microphase separation of binary liquids confined in cylindrical pores," *J. Phys. Chem. C* **120**, 9245–9252 (2016).
- ⁴⁹A. R. A. Hamid, R. Mhanna, P. Catrou, Y. Bulteau, R. Lefort, and D. Morineau, "Multiple glass transitions of microphase separated binary liquids confined in MCM-41," *J. Phys. Chem. C* **120**, 11049 (2016).
- ⁵⁰D. A. Kofke and E. D. Glandt, "Nearly monodisperse fluids. I. Monte Carlo simulations of Lennard-Jones particles in a semigrand ensemble," *J. Chem. Phys.* **87**, 4881–4890 (1987).
- ⁵¹D. A. Kofke and E. D. Glandt, "Monte Carlo simulation of multicomponent equilibria in a semigrand canonical ensemble," *Mol. Phys.* **64**, 1105–1131 (1988).
- ⁵²A. Z. Panagiotopoulos, "Monte Carlo methods for phase equilibria of fluids," *J. Phys.: Condens. Matter* **12**, R25 (2000).
- ⁵³V. K. Shen, J. K. Cheung, J. R. Errington, and T. M. Truskett, "Coarse-grained strategy for modeling protein stability in concentrated solutions. ii: Phase behavior," *Biophys. J.* **90**(6), 1949–1960 (2006).
- ⁵⁴K. S. Rane, S. Murali, and J. R. Errington, "Monte Carlo simulation methods for computing liquid-vapor saturation properties of model systems," *J. Chem. Theory Comput.* **9**(6), 2552–2566 (2013).
- ⁵⁵A. Z. Panagiotopoulos, *Gibbs Ensemble Techniques* (Springer, 1995), pp. 463–501.